ULTRASONIC ENHANCEMENT OF PULSED ELECTROCHEMICAL MACHINING

A Thesis

by

JIGAR BIMAL PATEL

Submitted to the office of Graduate and Professional Studies of
Texas A&M University
in partial fulfillment of the requirements for the degree of

MASTER OF SCIENCE

Chair of Committee,	Satish Bukkapatnam
Co-chair of Committee,	Wayne Hung
Committee Member,	Shiren Wang
Head of Department,	Mark Lawley

December 2016

Major Subject: Industrial Engineering

ABSTRACT

Electrochemical machining (ECM) has gained prominence in the field on precise machining and has been subjected to a lot of study in order to bring its use to commercial levels. One of the key issues of electrochemical machining is the lack of proper flushing ECM by-products. Ultrasonic assisted ECM is often used to minimize the flushing issue. This study attempts a novel variation in ultrasonic assistance of ECM by introducing ultrasonic waves in the flowing electrolyte without vibrating tool or workpiece. This ensures intense agitation in the inter-electrode gap (IEG) with relatively simpler set-up. Aluminum 6061 is used as a workpiece material to drill holes. Stainless steel tubes coated with Teflon is used as tool. The Teflon coating minimizes the effect of stray current.

Use of pulsed DC current and ultrasonic vibration improves the quality of the ECM'ed holes. The intense ultrasonic cavitation disturbs the anodic reaction in IEG negatively affecting MRR. On the other hand, the de-agglomeration of ECM by-products and depassivation of anodic workpiece improves surface roughness by approximately 50 % and the taper angle of the hole by approximately 75%.

ACKNOWLEDGEMENTS

I would to thank my mother, Swati Patel and father, Bimal Patel for their encouragement. All my accomplishments are due to their endless motivation and their untiring efforts to give me the best of opportunities in life.

I would like to thank Dr. Hung for the opportunity to work on this study. His guidance, support and motivation has been crucial in the completion of this work. I would also like to thank Dr. Bukkapatnam and Dr. Wang for their guidance and support throughout the course of this research.

I would like to thank my colleague, Zhujian Feng, in micro/nano manufacturing lab for helping me throughout this research study.

Thanks also go to my friends and colleagues and the department faculty and staff for making my time at Texas A&M University a great experience.

TABLE OF CONTENTS

Page

LIST OF FIGURES

Page

LIST OF TABLES

NOMENCLATURE

CFD	Computational Fluid Dynamics
CI	Confidence interval
EBM	Electron Beam Machining
ECDM	Electrochemical Discharge Machining
EDM	Electrical Discharge Machining
EMM	Electrochemical micro-machining
IEG	Inter-electrode gap
LBM	Laser Beam Machining
SEM	Scanning Electron Microscope
UEMM	Ultrasonic-assisted Electrochemical Micro-machining
WEDM	Wire-Electrical Discharge Machining

1. INTRODUCTION

Development of non-traditional machining processes was due to the realization that traditional processes like drilling, turning and milling have their limitations due to material removal by physical contact. One of the major limitations of conventional machining is to have the cutting tool material harder than the workpiece material. In the recent years, the requirement of machining accuracy, surface quality and the need to machine hard materials has increased tremendously. This need is particularly clear in medical device and aerospace industries. In medical device manufacturing, material removal by physical contact maybe detrimental because of contamination and significant subsurface damage. Conventional machining processes like drilling and milling require deburring to be performed separately, which may be difficult for complex features.

Non-traditional machining processes use thermal, electrical, chemical, mechanical energy. However, material is not removed using physical contact of a sharp cutting tool like conventional machining. Because of this features machined with non-traditional process have certain advantages.

For instance, non-traditional machining processes enable the machining of materials that are difficult to machining by conventional methods. Titanium and tungsten are notable examples. Due to the contact of cutting tool with the workpiece, surface defects are much more prominent in traditional machining. Non-traditional machining processes, specifically electrochemical machining (ECM) machine with almost no subsurface defects.

Non-traditional machining processes also enable the fabrication of complex geometric features which are normally difficult to machine with conventional methods. The ability of Wire-Electrical Discharge Machining (WEDM) machines to machine complex features is a notable example. This requirement is particularly of importance in the electronics industry, where there are often complex micro-features.

Different non-traditional machining processes have their own set of advantages and disadvantages. Electrical Discharge Machining (EDM) produces features but the biggest limitation of EDM is the thermal effects causing surface damage. Processes like Laser Beam Machining (LBM), Electron Beam Machining (EBM) and Ultrasonic Machining (USM) offer high dimensional control but very low material removal rates. Compared to these processes, ECM offers good material removal rates, dimensional control, surface finish and almost negligible surface damage.

For this reason, ECM has been identified as one of the most promising non-traditional machining process.

ECM is an anodic dissolution machining process where workpiece is anode and tool is cathode. When cathode and anode are placed in contact with electrolyte solution and current passed through the circuit, metal ions are removed from the anode. In this manner, different features are fabricated on workpiece (anode).

The is negligible tool wear and surface damage to the work-piece, making ECM advantageous over conventional processes where tool wear is a major concern. ECM also gives burr-free features and easily machines hard-to-machine materials as long as they are conductive.

However, to apply ECM in mass production, there are several issues that need to be solved. The biggest problem in ECM, especially with deep hole drilling using ECM, is the disposal of electrolyte sludge. Improper flushing of electrolyte slows down the anodic dissolution rate, promotes formation of passivation layer, and negatively affects the dimensional accuracy of machined feature.

This project studies a new approach to improve flushing of debris and subsequently improve hole quality during machining by ECM. This approach uses ultrasonic waves applied to flowing electrolyte during machining. The outcome of this method was observed on the Material Removal Rate, surface finish and hole taper.

1.1 Motivation

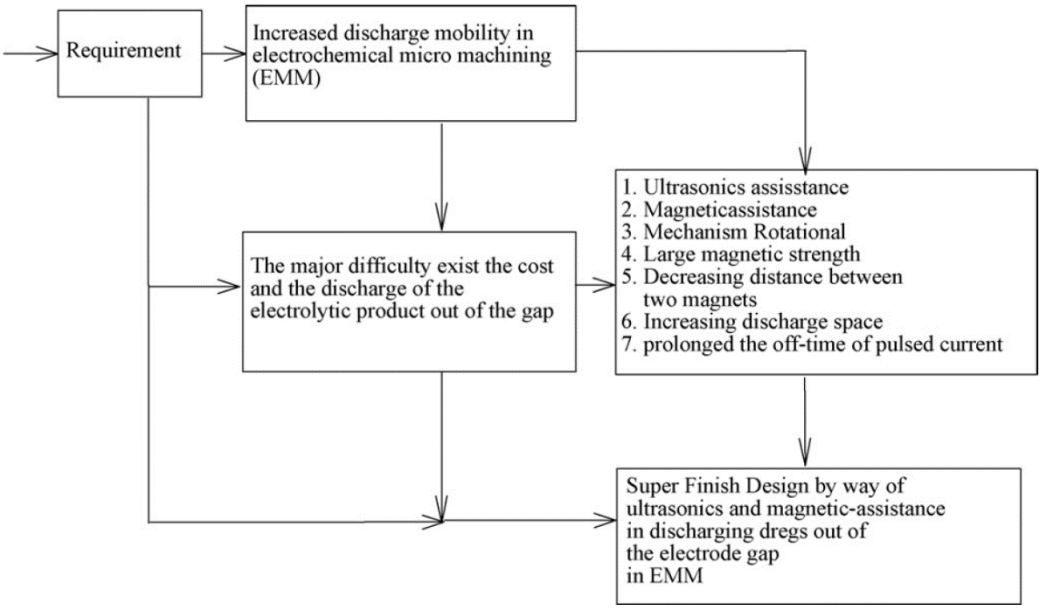

Figure 1: System Design Requirements and Major Issues in Electrochemical Micro-Machining (EMM). Reprinted from Pa (2009).

A lot of research has been done in ultrasonic enhancement of ECM and EDM to solve issues of conventional ECM (Figure 1). However, the ultrasonic enhancement of ECM by generating ultrasonic field in the electrolyte is an area that has not been explored as much as vibration of tool/workpiece has. Also, the electrochemical cells which enable high frequency vibration for either workpiece/tool require the mounting of an ultrasonic head on them. This increases the set-up complexity and cost. Moreover, ultrasonic vibration of the tool or work might not be purely longitudinal in reference to the feed direction, and slight transverse vibration might bring about dimensional

inaccuracies for the feature being machined. Lastly, since vibration is externally provided to the electrolyte itself, the vibration of the tube supplying electrolyte cannot influence the ultrasonic vibrations significantly.

The idea is that the cavitation imparted to the flowing electrolyte will cause the collapse of bubbles near machining area removing machining products accumulated in the IEG or in the machined feature.

With a relatively easier set-up, ultrasonic field can be generated close enough to the machining area to reduce the effect of machining products remaining suspended in the IEG. This is the motivation of this research. A laboratory set-up has been developed for the same.

1.2 Objectives and Scope

The scope of this study is limited to electrochemical machining of aluminum using hollow stainless steel tubes as tool. The electrolyte used for ultrasonic enhancement is a potassium bromide (KBr) at constant concentration and flow-rate. Pulsed DC current with variable frequency and amplitude is used to drive the electrochemical reactions.

The primary objectives of this study are:

1. Design and incorporate an ultrasonic actuator to the existing laboratory ECM system.

2. Study the influence of ultrasonic waves on ECM and how it affects MRR of workpiece and quality of machined surface.

2. LITERATURE REVIEW

2.1 Principle of ECM

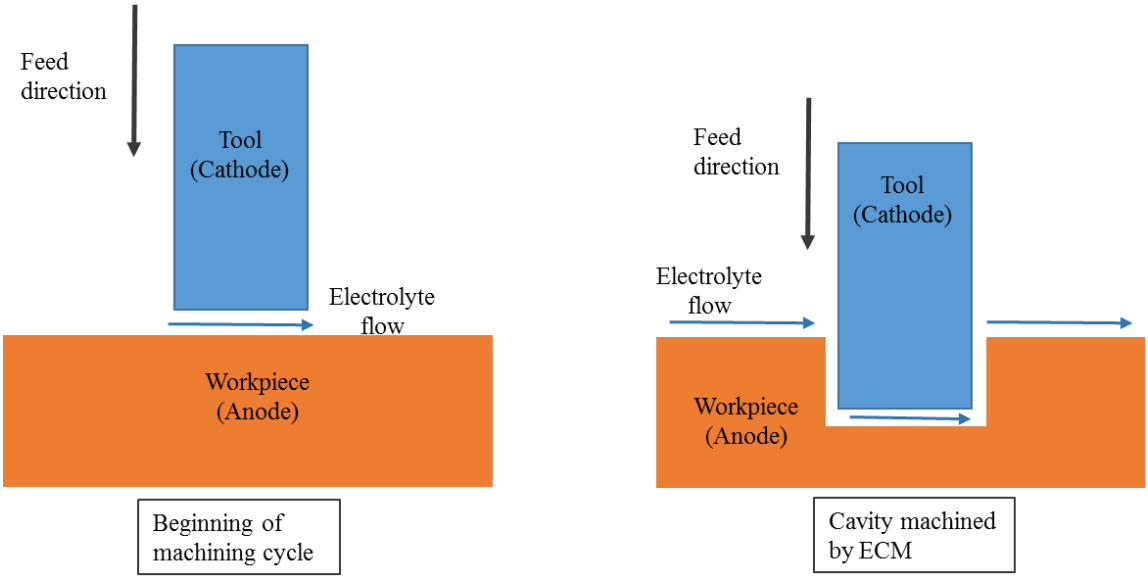

Figure 2: Principle of Electrochemical Machining

Electrochemical machining comes from the concept of electroplating, where anode material is plated on the cathode by ion transporting and flow of current (Figure 2). However, it was seen that if there is constant flushing of the electrolyte between cathode and anode then the material does leave the anode, but is not deposited on the cathode.

On proper design of cathode, the anode material is then left with a cavity that is the negative mirror image the anode shape. This process is called electrochemical machining (Bhattacharyya et al., 2004).

The cathode is the tool and the anode is the workpiece. The common area between the workpiece and the electrode is known as the machining zone and the IEG between the workpiece and the tool is known as the IEG.

The electrolyte is pumped at the machining area at high velocities in order to remove the machining products and remove heat. The IEG is an important factor in obtaining a good material removal rate. Also with the reduction of the IEG, the feature that is being machined has better geometric resolution since the influence of stray current is limited.

Research also highlights the importance of mass transport of ions being key to effective machining. and passivation layers on the workpiece surface is known to reduce the rate at which ions leave the anode and are flushed away. Mass transport can also be tied back to current density, which is the current generated in the IEG per unit cross sectional area.

2.1.1 Theory of ECM

Material removal rate (MRR) in ECM is derived from Faraday's Laws of electrolysis.

$$\mathbf{MRR} = \frac{V}{t} = \left(\frac{M}{zFd}\right)\left(\frac{EA}{gr}\right) = C\left(\frac{EA}{gr}\right) = CI \qquad \textbf{(1)}$$

Where,

MRR : material removal rate (mm^3/min)

V : removal volume at anode (mm^3)

t : processing time (min)

M : Atomic mass of anode (g/mol)

F : Faraday's constant = 96500 Coulomb

z : valency of anode material

d : density of anode material (g/mm^3)

I : working current (A)

E : voltage across electrodes (v)

A : effective area between electrodes (mm^2)

g : inter-electrode gap (mm)

r : resistivity of system (Ω cm)

C : specific removal rate (mm3/min/A)

Where, ρ = density of the material.

2.1.2 Advantages and issues of ECM

The advantages of ECM are realized by the ability of the process to machine materials that are usually hard to machine with conventional machining processes. The flexibility in tool selection is a major advantage. As long as it is conductive, any kind of workpiece can be machined by any tool material, provided the appropriate electrolyte is selected. This enables machining of hard materials with relatively "soft" tools. The tool wear in an ideal ECM process is zero. But even in practical applications, the tool wear is negligible, saving a lot of set up and tool changing costs. The electrolyte used to complete the electrical circuit can be filtered and reused in subsequent machining, thus saving cost in procuring electrolyte.

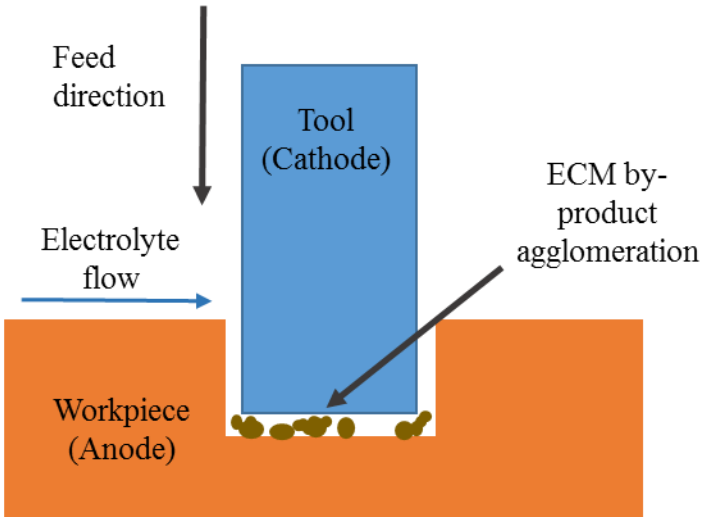

Figure 3: Agglomeration of ECM By-Products

The biggest limitation of ECM is that only electrically conductive materials can be machined and that too at a slower MRR compared to equivalent traditional machining processes. Slow MRR is one of the major reasons profound commercialization of ECM has not been seen yet. Another key issue is the corrosive property of commonly used electrolytes. Lastly, the outcome of machining by ECM often lead to poor quality of surface and dimensional accuracy because of agglomeration of ECM by-products in IEG (Figure 3). These by-products are detrimental to process stability because they short circuit the tool and the workpiece by bridging up the IEG. The agglomeration also reduces the rate of ion transportation reaction thereby reducing MRR. Therefore, improvement of flushing of these by-product is a key issue in need to be addressed.

2.1.3 Applications of ECM

Electrochemical Machining has the potential to replace most of the traditional applications like deburring, shaping, drilling and grinding, etc. This study is based on the drilling application of ECM, as explained below.

Drilling can be performed using any conductive metal tube or pin of appropriate diameter as cathode and feeding it into the workpiece (anode). In presence of current and flowing electrolyte, a hole will be fabricated roughly the same size as diameter of cathode. Use of tube shaped cathode (Figure 4), allows opportunity to use through-the-tool electrolyte flow which improves flushing. Also, the cross sectional area of tube is lesser than a solid rod. Thus, the current density of the former is higher.

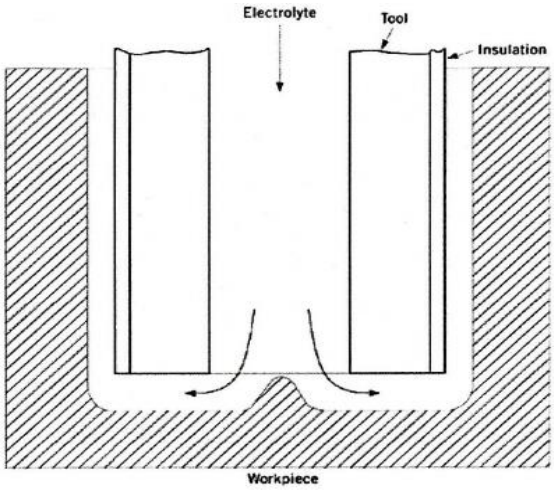

Figure 4: Drilling By ECM. Reprinted from McGeough (2005)

2.2 Parameters of ECM

The process of ECM is affected by several parameters. However, IEG, feed-rate, electrolyte, and power source are key factors that have a major effect on the outcome of ECM. These factors are discussed below:

2.2.1 Interelectrode gap

The role of IEG and the phenomena happening in it is crucial to the outcome of electrochemical machining. Controlling the IEG, the variation in the IEG and maintaining the desired conditions in the IEG can lead to a vastly improved dimensional accuracy and material removal rate.

According to Rajurkar et al. (1995), the variation in pulse voltage is linearly correlated to the IEG size. Hence it should be noted that any phenomena that influences either the IEG size or an inclusion of some machining products in the IEG will be reflected in the way voltage fluctuates during machining.

2.2.2 Feed-Rate

Higher feed rates would lead to better MRR since more material is removed in lesser time. (Wang et al. (2010), Ebeid et al. (2004), Swain et al. (2012), Rao et al. (2014)). However, it must be noted that this happens within the constraints of the rate of anodic dissolution and the rate of flushing of machining products.

Feed rate should be seen as an attempt to maintain the IEG and not as an actual way to increase the rate of machining. The rate of machining is governed by the speed at which ions leave the anode surface and also at the flow rate of electrolyte and the time allowed for it to flush these ions out of the IEG.

If the feed rate is higher than any of these rates, it will result in variation in IEG and in extreme cases it will cause contact between tool and workpiece, resulting in short circuiting.

2.2.3 Electrolyte

The electrolyte performs the function of completing the electrical circuit between cathode and anode. However, the circulation of electrolyte in an effective manner is also vital for ECM process.

Although the machining products might not directly be a factor influencing ECM process efficiency, the existence of ECM by-products of electrochemical reaction staying in the IEG might short circuit the cathode and anode, causing sparks and damaging both the tool and work piece. Such discharges also make the process unstable in terms of maintain the IEG or the variations and sudden surges in voltage, etc. Hence it

is desirable to have flowing electrolyte which can flush away all the electrolyte in the IEG and all the machining products with it.

It is desirable to have electrolytes with low throwing power. Low throwing power means that the ability of the electrolyte to plate uniformly to an irregularly shaped cathode is weak. Since no plating or deposition of ions on cathode (tool) is desired, it makes sense to prefer low throwing power in ECM.

Mukherjee et al. (2008) used 1.5 M sodium chloride (NaCl) as electrolyte with a goal to observe the change in valency of aluminum during machining and its effect on MRR. Higher concentration of electrolyte might increase the rate of ion removal from anode, but that might also be detrimental to the accuracy of machining as stray machining might happen.

The toxicity of electrolytes is a major cause of concern towards widespread implementation of ECM. However, use of citric acid as electrolyte to achieve environment-friendly ECM is one of the attempts to overcome this limitation (Ryu, 2015).

According to McGeough (1974), the voltage required to break down passive films on workpiece is reduced by use of bromide or iodide electrolytes. However, poor finish is to be expected in this case.

2.2.4 Voltage

A lot of initial research and development showed the potential of using pulsed current instead of continuous current in electrochemical machining (Figure 5).

With excessively high current density, too many ions leave the anode surface. The amount may be way too much to be flushed all at the same time, which leaves machining products in the narrow IEG. Gradually as the machining progresses, this might cause buildup of anode material on the tool. The likelihood is that this deposition is not uniform, and hence the rate of anodic transportation is no longer uniform, resulting in the distortion of the geometric profile of the feature being machined.

With pulsed current machining, there is on-time and off-time for peak current to be achieved. The off-time is crucial for the flushing away the material removed during on-time so as to begin the next on-time phase with fresh electrolyte in the IEG every time and minimal deposition on the tool.

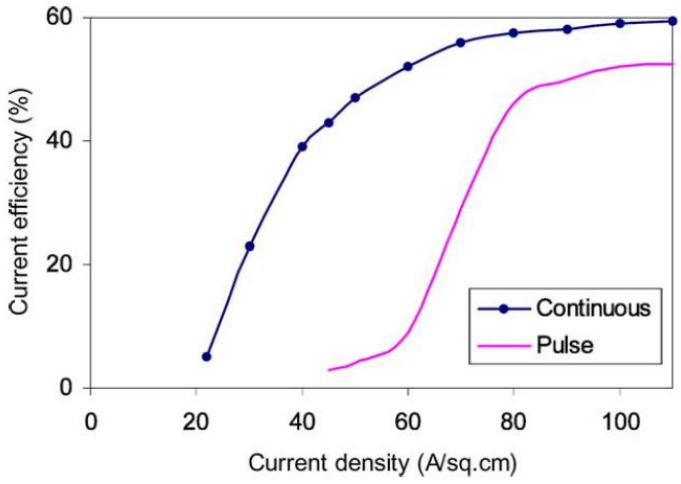

Figure 5: Comparing Current Density Vs Efficiency for Pulsed and Continuous Current. Reprinted from Bhattacharyya et al. (2004).

2.3 Ultrasonic Waves and Cavitation

Ultrasonic waves have a restively short wavelength which results in a very narrow beam. High frequency (in the order of at least kHz) has led to several interesting applications of ultrasonic waves, mainly due to the phenomenon of cavitation.

Cavitation occurs due to presence of strong ultrasonic fields in liquids. It is the formation and subsequent collapse of "micro-bubbles" in the liquid (Kuttruff, 2012). The asymmetric collapse of these bubbles results in micro-jets in the liquid and the symmetric collapse results in shockwaves. (Yusof et al., 2016)

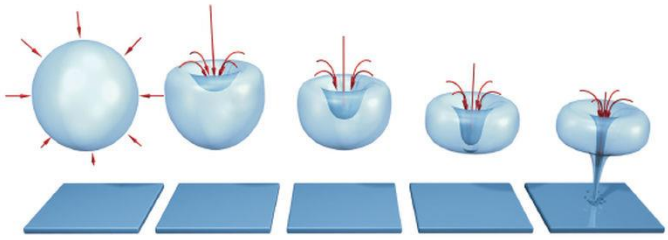

Figure 6: Micro-Jet Formation Due to Asymmetric Collapse of Cavitation Bubble. Reprinted from Wess (2006)

As seen in the Figure 6 above, the collapse of a single bubble near a wall or any solid boundary occurs because of asymmetric radial pressure around the bubble. The surface of the bubble farthest from the wall experiences deformation due to this and it eventually causes an implosion and evolution of the jet (Kuttruff, 2012). According to Aglyamov et al. (2008), the life of cavitation micro-bubbles in water is a little over 140

μs. However, the high vapor pressure of electrolytes compared to that of water may slow down the time taken for the collapse.

Verhaagen et al. (2016) described a study of how cavitation bubbles clean using advanced techniques and instruments such as high-speed imaging, son luminescence recordings, and surface cleaning tests. Two distinct bubble groups were identified. The bubbles with sizes larger than linear resonance size are in the plane parallel to the surface of the transducer, whereas the ones that are smaller are all perpendicular to the transducer surface. The smaller bubbles are farther away from the transducer from the large ones and behave as streamers. Both bubble groups reported cleaning, according to the authors, however the exact cleaning mechanisms could not be predicted. The streamer bubbles seemed to clean from the small crevices as well (Xi et al., 2011).

Figure 7 depicts different stages of two different kinds of cavitation. Micro-jets and shockwaves are a result of transient cavitation whereas the scrubbing action is due to the stable cavitation. Skoczypiec (2010) believes that it is transient cavitation that is of interest with regards to ECM.

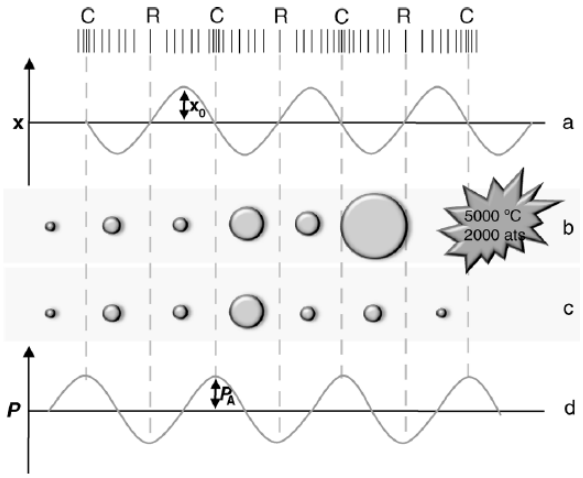

Figure 7: Creation of Cavitation Bubbles and Their Collapse. (A) Displacement Graph, (B) Transient Cavitation, (C) Stable Cavitation, and (D) Pressure Graph. Reprinted from Capelo-Martinez (2009).

2.3.1 Factors affecting ultrasonic vibration and cavitation

2.3.1.1 Frequency

McQueen (1986) compared the efficiencies of cleaning systems with 2 different frequencies, one at 40 kHz and another at 220 kHz. This showed that removal of sub microscopic contaminants is better at higher frequencies whereas relatively larger contaminants are cleaned better in systems emitting relatively lower frequency.

This might suggest the use of higher frequency ultrasonic assistance when machining micro-profiles using ECM.

Another important note will be the idea of cleaning at extremely high frequencies of the order of MHz This is being termed as megasonic cleaning and it is gaining interest because cleaning at this order of frequency minimizes the damage caused to cleaning surface due to pitting. The reason given for this is that at frequencies this high, the sound field manages to interact directly with the particle to be removed without affecting the boundary. The second reason is that the microscopic bubbles generated at this frequency tend to resonate rather than collapse. This gives rise to a “scrubbing action” rather than the micro-jet or shockwave formation usually responsible for pitting.

2.3.1.2 Amplitude

The amplitude or maximum displacement of the ultrasonic transducer is proportional to the intensity of cavitation in the liquid. High amplitude may cause damage to the ultrasonic transducer and may cause liquid agitation instead of pure cavitation (Capelo-Martinez, 2009). However, for viscous liquids a higher amplitude is essential to promote cavitation effectively.

Low intensity ultrasound is typically used in analysis, testing and imaging applications whereas high-intensity ultrasound is used for processing applications such as mixing, dispersing and de-agglomeration (Hielscher, 2007).

2.3.1.3 Liquid

According to Capelo-Martinez (2009), a higher viscosity and surface tension of the liquid used inhibit cavitation. Because of this reason the commonly used liquid for such applications is water. Higher cohesive forces binding the liquid molecules make cavitation difficult to achieve (Mason et al., 2002). Organic solvents have historically been the fluid of preference due to the favorable cavitation conditions they provide in terms of viscosity, surface tension and vapor pressure (Mason, 2016).

2.3.1.4 Temperature

The role of temperature of liquid in achieving cavitation is two-fold. At higher temperatures, the number of active sites to promote cavitation increase and the forces binding the liquid molecules weaken. However, according to Mason (2000), better cavitation is achieved at lower temperatures, because at higher temperatures more solvent vapor fills the bubbles and that makes the collapse less violent and the cavitation is less intense than expected.

As per Niemczewski (1980) in case of water the best temperature for cavitation is 35 Celsius but with most other aqueous solutions cavitation is best in the range of 50 degrees Celsius and 65 degrees Celsius.

2.3.1.5 State of liquid

Studies show that with the presence of micro-bubbles of appropriate size present already before ultrasound is passed, increases the cavitation activity in the liquid significantly and also increases the amount of jetting action (Zijlstra et al., 2015).

If the liquid already contains dissolved gases, then it increases the micro-bubble formation (Li et al., 2015). Since this study applied ultrasonic vibration to flowing electrolyte, intense cavitation can be expected due to the presence of dissolved electrolyte gas and ECM by-products (Skoczypiec, 2010).

2.3.2 Safety and Health Risks related to ultrasonics

The effect of airborne ultrasound may result in hearing loss if there is constant exposure to ultrasound in the region of 20-25 kHz, however at 40 kHz there is no health risk in terms of hearing since the sound is well beyond hearing range (Kuttruff, 2012).

While using the ultrasonic probe, care must be taken to avoid touching the probe while it is vibrating, as it may cause injury.

2.4 Ultrasonic Enhancement of ECM

2.4.1 Passive films on anodic workpiece material

Passivation or anodic film formation is the rapid formation of thin oxide layer on workpiece surface during ECM. This layer firmly attaches to the workpiece surface and acts as a barrier to anodic dissolution (Hoar, 1967).

According to McGeough (1974), the passive film on titanium makes its ECM process difficult and requires higher voltage to machine through the passive films. Even in this case, the higher voltage will break the passive films only at its weak regions,

resulting in an uneven finish during ECM. The same issue was observed in ECM of tungsten carbide, where the cobalt present in the material forms a passive film.

According to Powers (1971), bromide and iodide electrolytes reduce the voltage required to break the passive film but still yield a poor finish.

Partial passivation was the reason for poor finish (CLA greater than 5.2 μm) and low current efficiency (40 μm) for ECM of cast iron (McGeough, 1971).

Past research has attributed this passive films to the unstable anodic dissolution and the subsequent variations in the current density. It is believed that the periodic formation and rupture is the cause of such fluctuations in current density (Postlethwaite et al., 1972).

Increase in voltage which subsequently increases the current density may transition the ECM process from machining in passive to the transpassive state (McGeough, 1974). ECM experiments by LaBoda et al. (1967) on low-alloy nickel-chromium steel that yielded surface roughness of 0.1μm were conducted in transpassive region. This transition from passive to transpassive state of ECM is influenced by the current density and electrolyte flow-rate (efficient flushing).

The anodic films which clearly affect the surface finish also affect the dimensional control of ECM process and the nature of such films different with different electrolytes.

2.4.2 Ultrasonic vibration of tool or workpiece

Bhattacharyya et al. (2007) studied the influence ultrasonic vibration of electrode on the output parameters of ECM. His study showed that the effect of ultrasonic vibration frequencies is not significant on MRR and overcut of ECM'ed micro-holes. As seen in Figure 8 and Figure 9, the frequency range of 3-23 kHz does not show any significant effect on MRR or overcut.

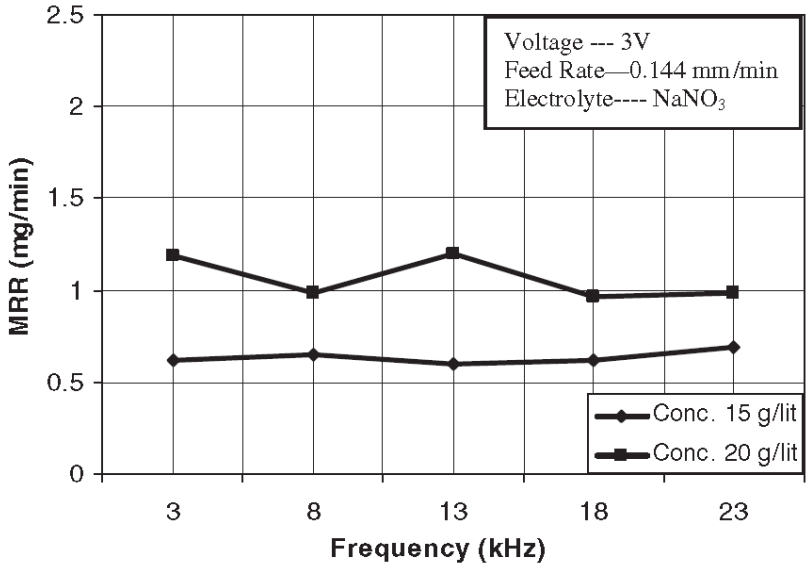

Figure 8: Influence of Ultrasonic Vibration Frequency On MRR. Reprinted from Bhattacharyya et al. (2007).

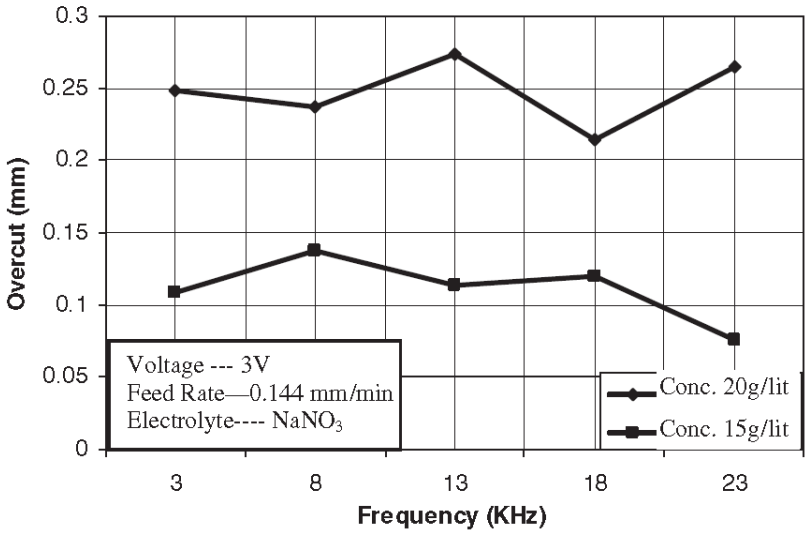

Figure 9: Influence of Ultrasonic Vibration Frequency On Overcut Reprinted from Bhattacharyya et al. (2007).

After further experiments in the low frequency range (of the order of Hz), Bhattacharyya et al. (2007) concluded that low frequency vibration was a better improvement technique than high frequency vibration.

However, the work of other researchers, described below. Provided with evidence of benefits of ultrasonic vibration in ECM.

Pa (2009) studied the influence of ultrasonic and magnetic fields on ECM in an attempt to achieve superfinishing. Tool vibration at very high frequencies was studied, ranging between (46-120 kHz). Results showed that using very high frequencies improves surface finish by approximately 0.20 µm (Figure 10) .

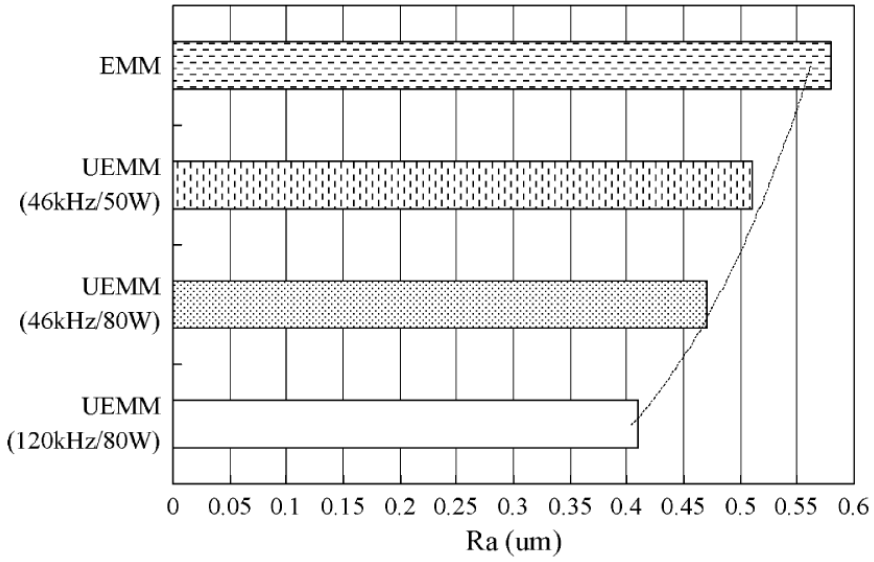

Figure 10: Effect of Ultrasonic Vibration Frequency and Power on Surface Roughness during UEMM (Ultrasonic-Assisted Electrochemical Micro-Machining) Reprinted from Pa (2009).

In another study to achieve superfinishing, Pa (2006) used a rotating workpiece and different designs of electrode along with ultrasonic vibration and pulsed DC current (Figure 11). The frequency and power of ultrasonic vibrations was 46 kHz/50W, 46 kHz/80W, 120 kHz/80W, and 120 kHz/150 W. The pulse period (on/off time) was 100 ms/100 ms, 100 ms/200 ms, 100 ms/300 ms, 100 ms/400 ms, and 100 ms/500 ms.

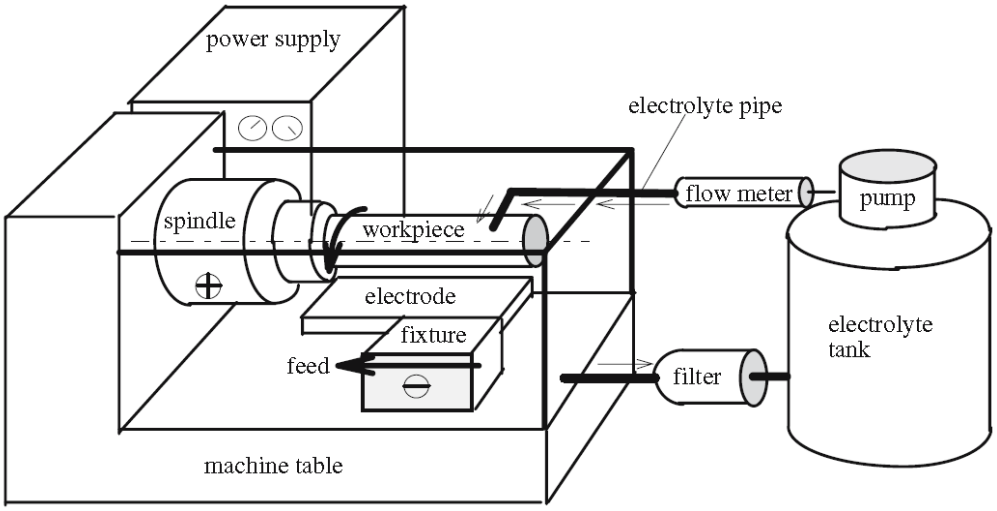

Figure 11: Set-Up for Surface Smoothening Using ECM. Reprinted from Pa (2006).

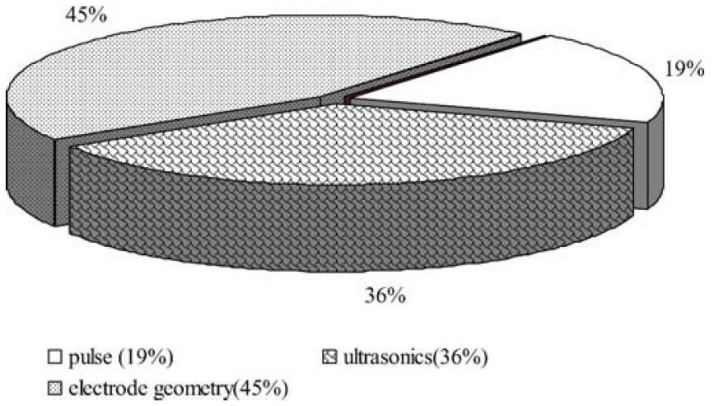

Figure 12: Contribution of Different Factors Towards Surface Finish. Reprinted from Pa (2006).

Research work by Pa (2007) to improve surface finish of drilled holes led to conclusion that use of pulsed DC current is crucial to flushing of ECM by-products. However, it was also observed that use of novel electrode design and ultrasonic vibrations can save the cost of implementing pulse DC power source (Figure 12).

Ruszaj et al. (2001) reported an improvement in surface quality by ultrasonic vibrations of tool during traditional ECM process (Figure 13). The workpiece machined was NC6 steel with brass as the electrode. The power of ultrasonic vibrations was varied between 20-120W with a maximum amplitude of 10μm.

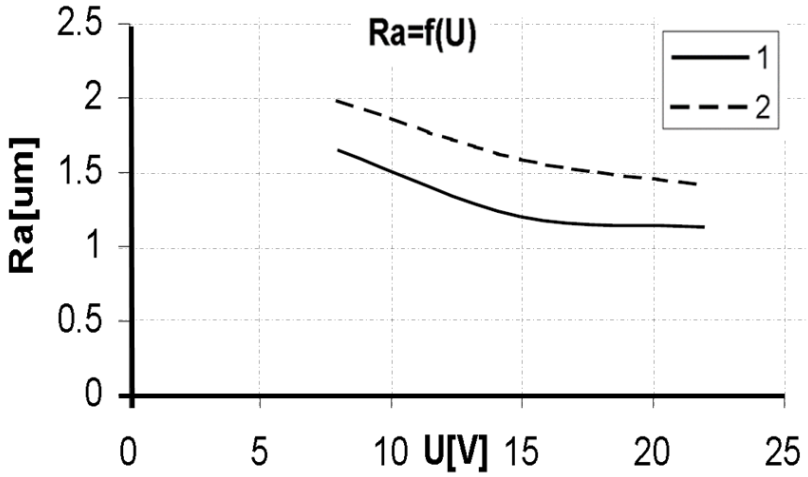

Figure 13: Effect of Interelectrode Voltage on Surface Roughness. Curve 1: ECM with Ultrasonic Vibrations, Curve 2: ECM Without Ultrasonic Vibrations Adapted from Ruszaj et al. (2001).

In a study investigating ultrasonic vibration in ECM-CNC process, Sebastian et al. (2003) explained that the impact of micro-jets due to ultrasonic cavitation have significant effect on the chemical composition and physical morphology and therefore affect surface quality and dissolution rate.

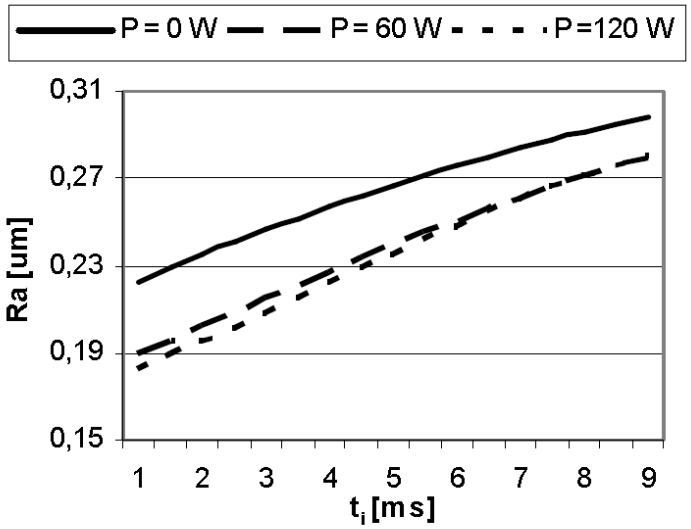

Figure 14: Influence of Power of Ultrasonic Vibrations and Pulse Time on Surface Roughness. Reprinted from Ruszaj et al. (2007).

Use of pulsed current and ultrasonic vibrations was used by Ruszaj et al. (2007), in an attempt to achieve polishing effect on NC6 steel. The power of ultrasonic vibrations was between 0-120W and pulse time was between 1-9 ms. Surface roughness (R_a) was measured to show surface quality and Figure 14 shows that best surface finish is achieved at high power of ultrasonic vibrations and low pulse time. Similar research was also carried out by Ruszaj et al. (2003) with NC6 steel as workpiece and ultrasonic tool vibrations (amplitude: 2- 11 µm) and it was concluded that there exists specific amplitude to give optimum surface finish in different machining conditions.

Skoczypiec (2010) performed simulations of Ultrasonically-assisted ECM (USAECM) using Computational Fluid Dynamics (CFD). In order to understand the influence of cavitation on the dissolution process, he solved the problem of electrolyte

flow when tool is vibrating at 20 kHz frequency and different amplitudes (up to 10 μm). The modelled IEG is shown in Figure 15.

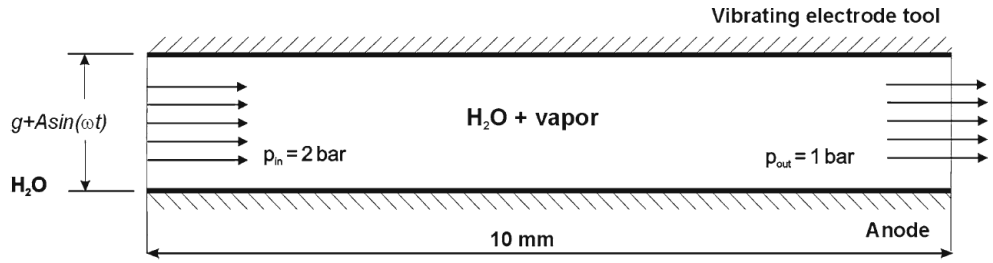

Figure 15: Modelling of IEG (1mm) With Ultrasonic Vibration of Tool Reprinted from Skoczypiec (2010).

The results of this simulation showed that the pressure of electrolyte in the IEG constantly changes due to the evolution and rapid collapse of cavitation bubbles (Figure 16).

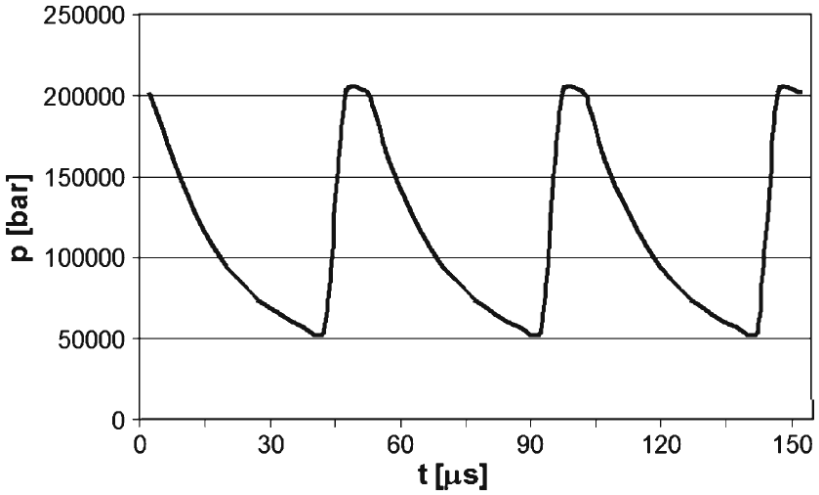

Figure 16: Pressure of Electrolyte Close to Anode Surface. Ultrasonic Vibration Amplitude 5 µm and Period of Vibration = 50 µs. Reprinted from Skoczypiec (2010).

Wang et al. (2016) used ultrasonic vibrations on a disk-shaped micro-tool for deep hole drilling experiments. The disk-shaped tool was to further enable better flushing.

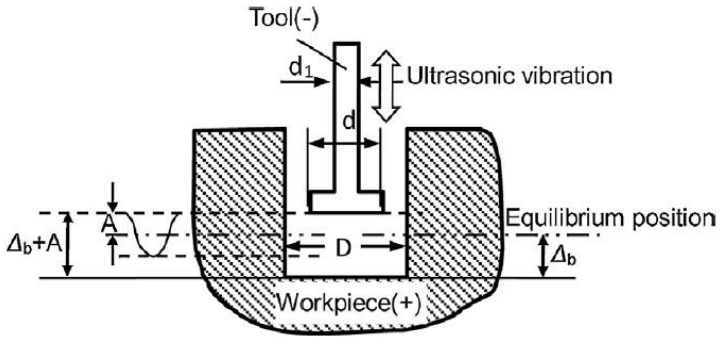

Figure 17: Schematic of a Disk-Shaped Tool. Reprinted from Wang et al. (2016).

The improvement in the ECM process by the ultrasonic vibrations was characterized by observing the change in overcut, which improved significantly (Figure 18).

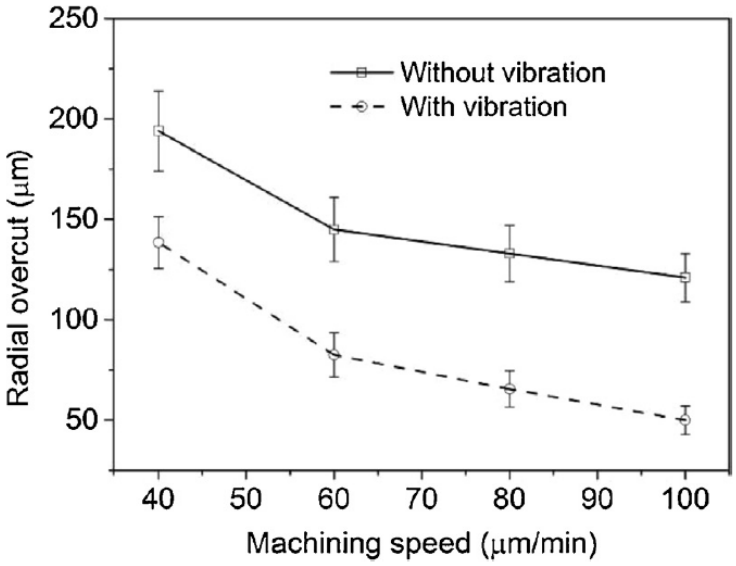

Figure 18: Radial Overcut at Different Machining Speeds for ECM With and Without Ultrasonic Tool Vibration. Reprinted from Wang et al. (2016).

This study also observed the movement of the tool driven by a feedback system that detected short circuit between tool and workpiece and immediately induced backward feed and re-adjusted the IEG size. The number of times this occurrence would happen speaks to the process stability and the number of occasions where the IEG reduces (due to vibration) but the machining products are still in the narrow IEG.

The experiments conducted logged the movement of the tool as it encountered short circuit between tool and workpiece. The results with tool vibration and without were compared as shown in Figure 19. It is clear that without the influence of ultrasonic vibration, the tool back feeds more than the instance where vibration is used. This points towards a greater process stability in the case where vibration is used.

The ultrasonic vibration of the tool narrows the IEG and widens it periodically. This causes the machining products to be forced out and fresh electrolyte to pour into the IEG periodically as well. Hence, effective flushing is evident.

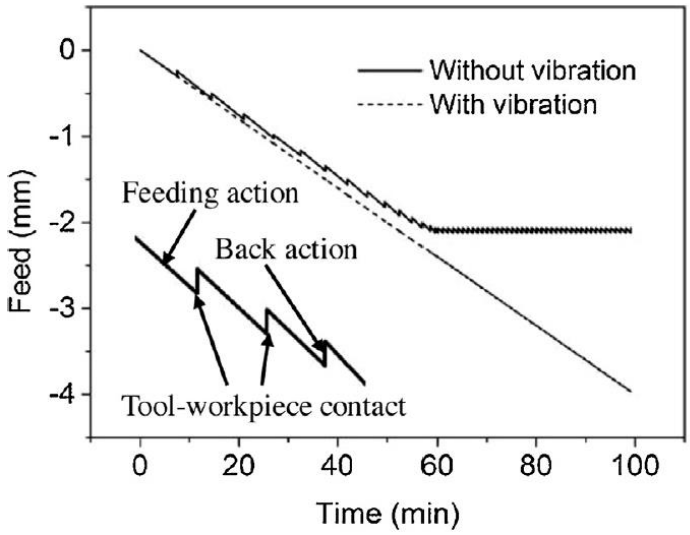

Figure 19: Process Stability Comparison with ECM Performed with and Without Use of Ultrasonic Vibrating Tool. Reprinted from Wang et al. (2016).

According to the study, the effect of ultrasonic vibrations changes drastically with the current/voltage values. It was noted that this could be owing to the IEG size.

The MRR is not at all affected by ultrasonic vibrations with the IEG thickness being large (Skoczypiec et al., 2005).

Mitchell-Smith et al. (2016) conducted Electrochemical Jet Machining (ECJM) on titanium. Vibration of workpiece was accomplished by utilizing a set-up as seen in Figure 20. 31% reduction in surface roughness (R_a) was obtained due to ultrasonic vibration. There was significant reduction in oxide layer formation by use of ultrasonic vibration 22% area of sample showed passive layer formation with use of ultrasonic vibration, compared to 36 µm area without vibration.

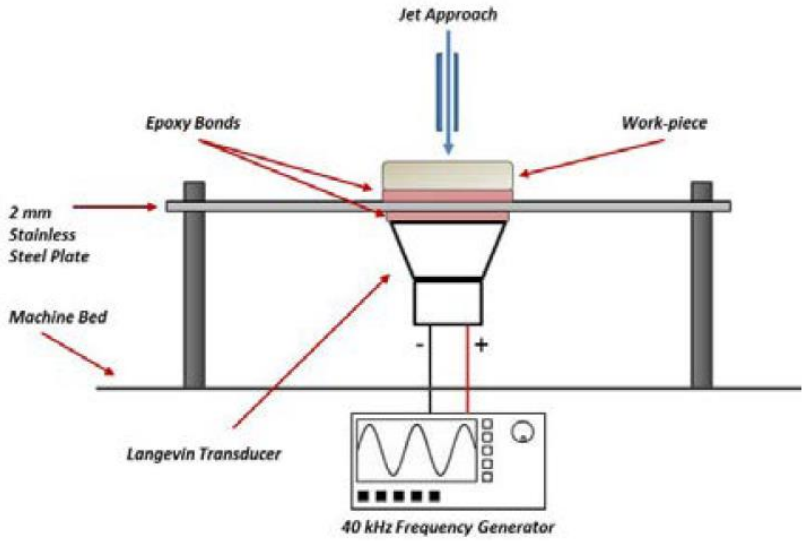

Figure 20: ECJM By Ultrasonic Vibration of Workpiece. Reprinted from Mitchell-Smith et al. (2016).

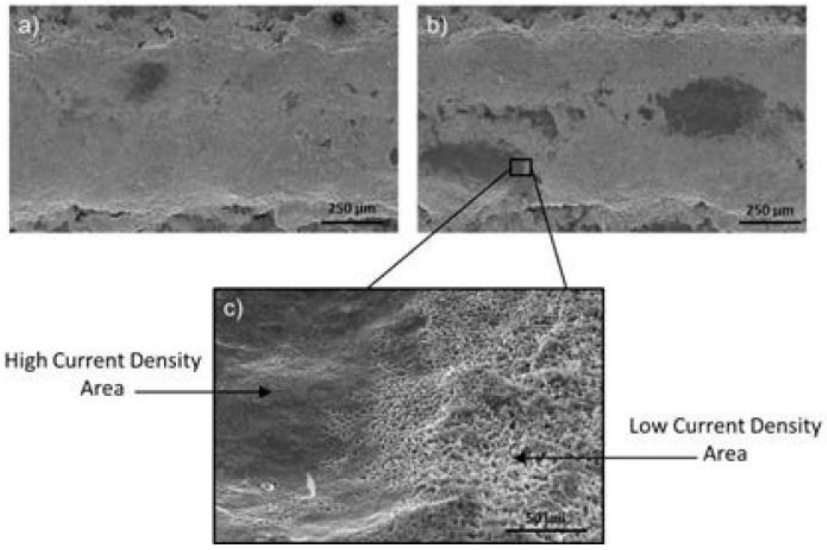

Figure 21: Increase in High Current Density Region (A) Without Ultrasonic Vibration, (B) With Ultrasonic Vibration, (C) Magnification of High and Low Current Density Region. Reprinted from Mitchell-Smith et al. (2016).

Figure 21 shows Scanning Electron Microscope (SEM) images of machined samples. It is clearly seen that ultrasonic vibration increases the high current density area, thereby improving surface quality.

2.4.3 Ultrasonic vibration of electrolyte

Nicoară et al. (2006) studied the effect of conducting ECM in ultrasonic field by setting up the Electrochemical cell in ultrasonic bath.

Using two ultrasonic baths of 20 kHz and 56k Hz were used and the effect of ultrasound was expected to transmit through the glass walls of the electrochemical cell (Figure 22).

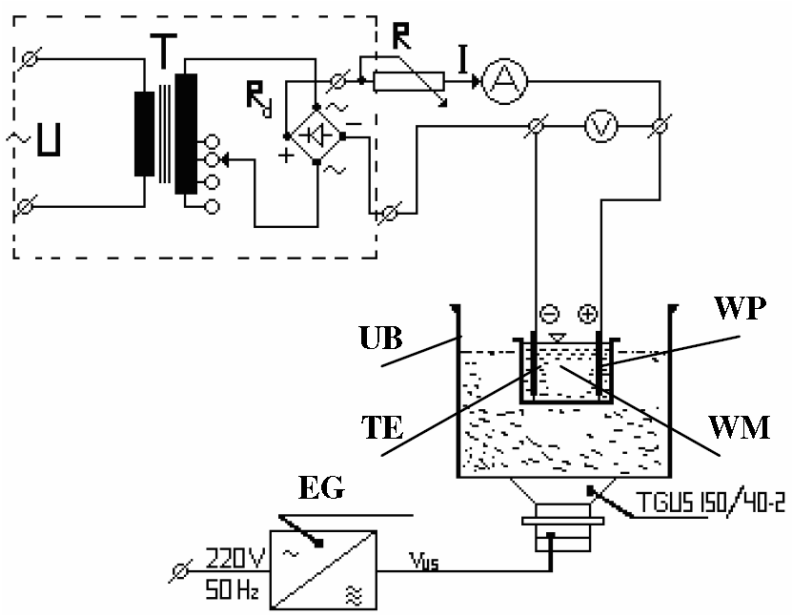

Figure 22: Use of Ultrasonic Bath to Enhance ECM. UB : Ultrasonic Bath, WP : Workpiece, TE : Tool Electrode, WM: Electrolyte, TGUS: Ultrasonic Transducer, EG: Electrical Generator. Reprinted from Nicoară et al. (2006).

This study showed some changes in the plot of voltage and current values with time under the influence of the ultrasonic field. The small increase in current over time was observed owing to the depassivation caused by ultrasonic field. An increase was also observed in material removal rate, with the increasing operating frequency of the ultrasonic bath (Table 1).

Current	10 A			15 A		
Probe	Control	20 kHz	56 kHz	Control	20 kHz	56 kHz
M[g]	1.946	1.972	2.014	3.014	3.064	3.096
MP[g/min]	0.194	0.197	0.207	0.301	0.309	0.309

Table 1: Influence of Ultrasonic Field on Material Removal. Reprinted from Nicoară et al. (2006)

This could be from the fact that the source of the ultrasonic field was too far from the IEG where the influence is required. The transducers of the ultrasonic bath would have to transmit ultrasound through the bath liquid, glass walls of the cell and finally carry cavitation to the narrow IEG. The possibility is that the cavitation effect weakens greatly by that time. This might suggest that for this particular application of enhancing ECM output, the cavitation through ultrasonic baths might not affect the process as it affects normal cleaning of samples.

Han et al. (2009) applied ultrasonic vibration to electrolyte to improve Electrochemical Discharge Machining (ECDM) process (Figure 23). An ultrasonic vibrator was placed under the workpiece in the electrolyte bath and ultrasonic vibration frequency was 1.7 MHz. The results are shown in Figure 24.

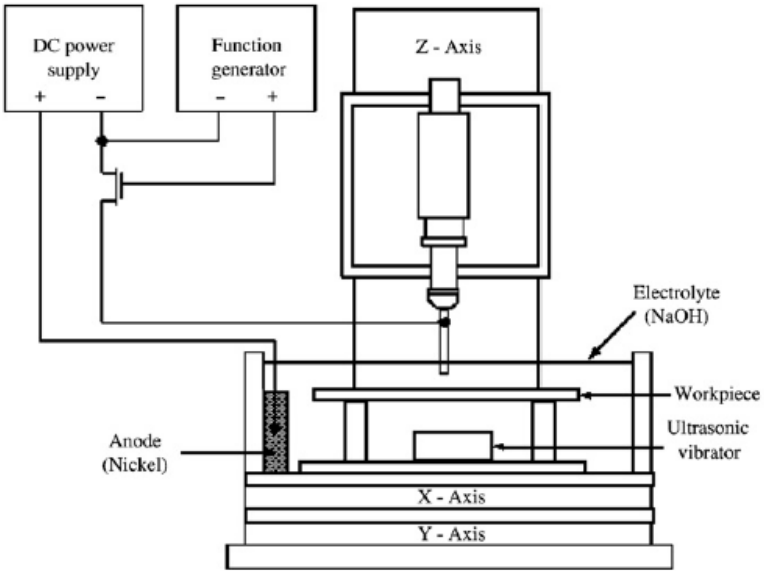

Figure 23: Ultrasonic Vibration of Electrolyte in ECDM Process. Reprinted from Han et al. (2009).

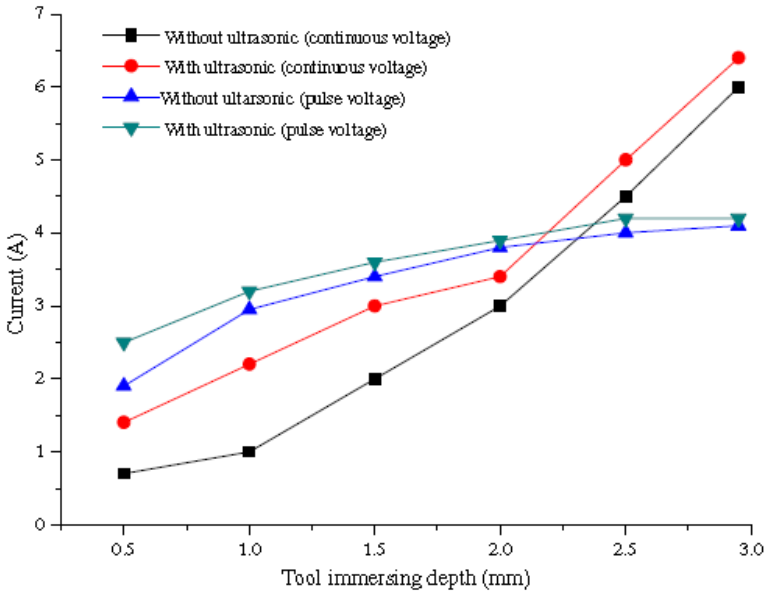

Figure 24: Influence Electrolyte Formation and Pulsed Voltage on Tool Depth. Reprinted from Han et al. (2009).

2.5 Summary of literature review

Use of continuous DC current has been a major factor behind lack of proper flushing. Constant anodic dissolution leaves insufficient time for the by-products in the IEG to be flushed and fresh electrolyte to be replenished. Physical conditions in the IEG are required to be stable in order to maintain uniform conductivity. Use of pulsed-current is beneficial to avoid elevated temperatures in IEG and also to allow proper flushing of ECM by-product.

Ultrasonic cavitation plays a crucial role in de-agglomeration of ECM by-products in the IEG, improved electrolyte replenishment and process stability. However, applying ultrasonic vibration to tools or workpiece has some limitations. Mounting a tool on ultrasonic head not only raises set-up cost of ultrasonic-aided ECM, but it also makes it difficult to incorporate though-tool electrolyte flow during ECM. The ultrasonic vibration of workpiece may also increase set-up cost, especially during machining of heavy workpieces. Lastly, the direct vibration of tool or workpiece increases the risk of dimensional inaccuracy of backlash of vibration. This limitation can be critical for precise machining application. Direct ultrasonic vibration of electrolyte may retain benefits of cavitation and overcome the above limitations.

3. LABORATORY SYSTEM

The existing laboratory set-up and the incorporation of the ultrasonic actuator is described in this section.

3.1 Experimental Set-up

Figure 25 shows the laboratory prototype of horizontal ECM system with an ultrasonic probe used in this study.

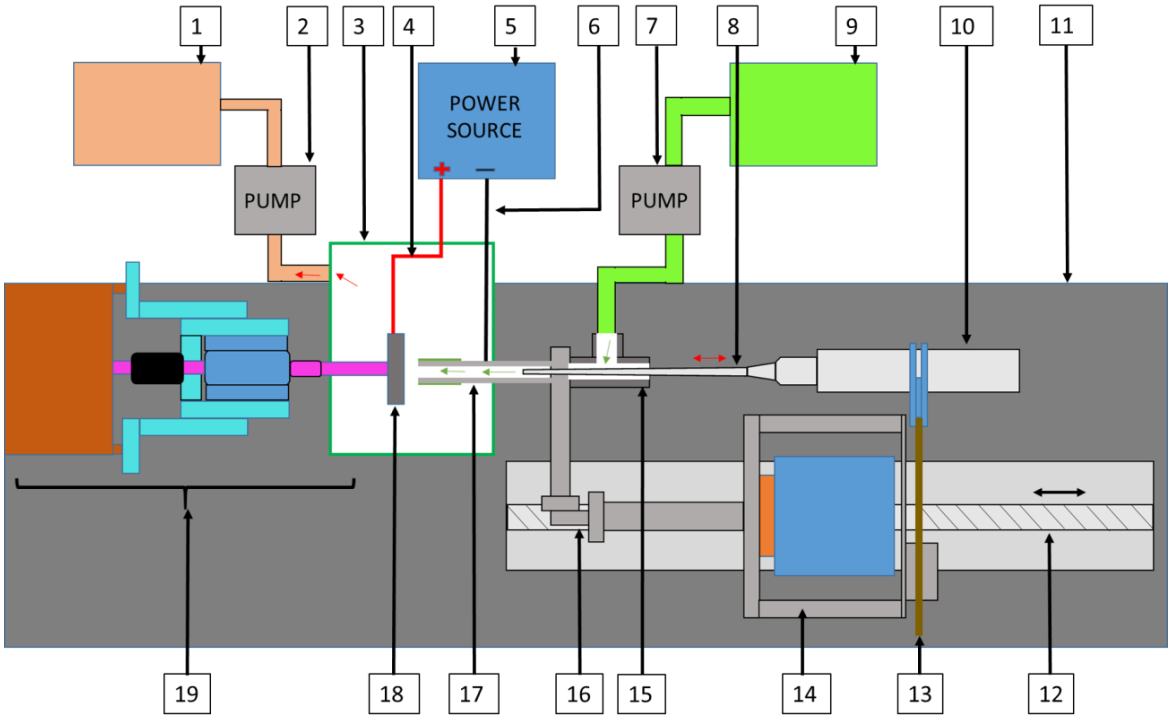

Figure 25: Laboratory Horizontal ECM System with Ultrasonic Probe System

The components of the ECM system are as follows.

1) Used electrolyte container
2) Longer WT2600-2J peristaltic pump
3) ECM cell
4) Anode terminal
5) Everlast 255EXT power supply
6) Cathode terminal
7) Longer WT2600-2J peristaltic pump
8) Detachable Branson SLPe probe
9) Fresh electrolyte container
10) Branson SLPe ultrasonic convertor
11) Granite table
12) Velmex BiSlide positioning system
13) Four finger extension clamp
14) Fixture for ultrasonic actuator
15) Tee pipe-joint
16) Tool attachment fixture
17) Teflon coated stainless steel tool
18) Workpiece
19) Labworks ET-132-2 low frequency vibrator

The entire system rests on a granite table (11) to minimize vibration and maintain rigidity during set-up. The existing laboratory system is designed so that the tool moves horizontally into the workpiece while machining. This is done to improve flushing of electrolyte from the IEG. The workpiece is clamped on a fixture that has been coupled with a low frequency vibrator (19). For this study the low frequency vibrator is not used.

The workpiece is clamped inside a plastic ECM cell (5). The stainless steel tool is mounted on the Velmex positioning system (12). Using attachment (16) the axis of the tool is offset from the axis of the Velmex positioning system (12). This is done to allow the ultrasonic probe to be inserted into the hollow tool using fixture (14) and universal clamp (13). As seen in the figure above, when the Velmex positioning system moves along the lead screw, the tool and the ultrasonic actuator moves along an axis parallel to the Velmex system and into the workpiece (18). A pair of peristaltic pumps, (2) and (7) circulate electrolyte to and from the ECM cell. Used electrolyte is collected in container (1) while fresh electrolyte is pumped from container (9). Appropriate wiring, (4) and (5), connects workpiece (anode) and tool (cathode) to the power source (5).

Detailed description of each component can be found in Appendix B.

3.2 Ultrasonic actuator system

The following requirements were sought for incorporating an ultrasonic actuator in the horizontal laboratory ECM system:

1) The direction of vibration of probe should be along the direction of the tool feed
2) Ultrasonic waves should be close to the IEG so as to allow optimal flushing during deep hole fabrication

Considering these two requirements, the ultrasonic probe was incorporated on the Velmex system as seen in Figure 26.

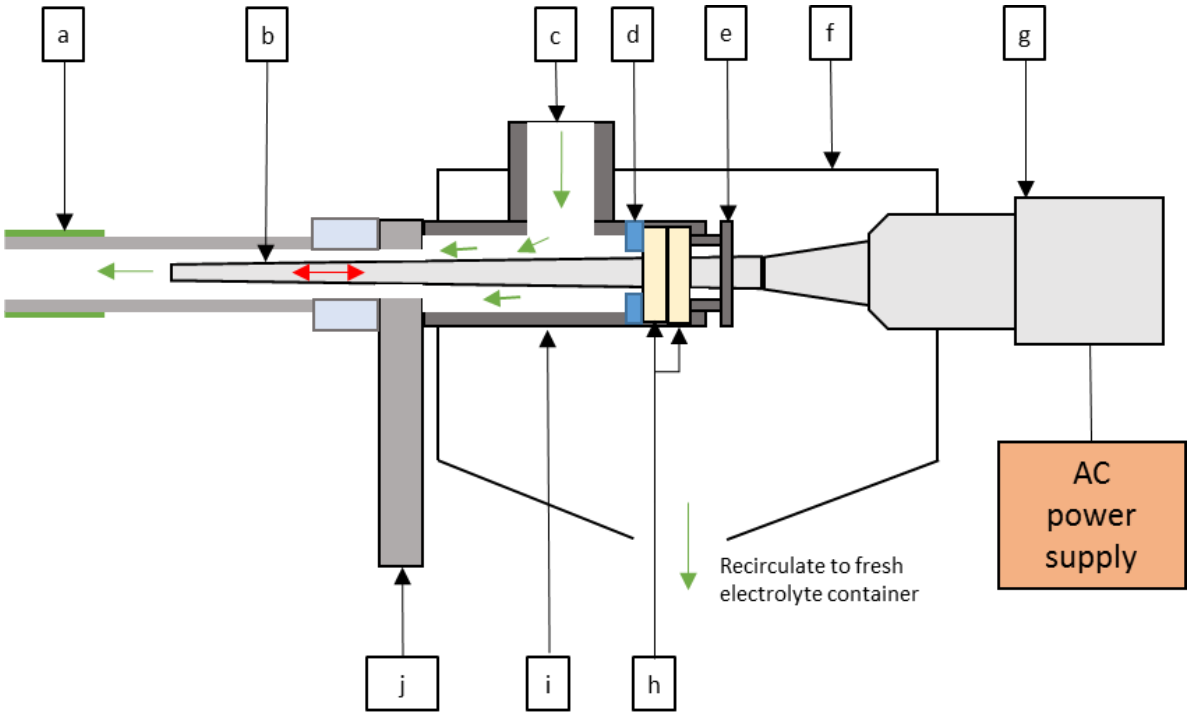

Figure 26: Schematic Showing Incorporation of Ultrasonic Actuator

a) Teflon coated stainless steel electrode
b) Branson SLPe ultrasonic probe
c) In-flow of fresh electrolyte
d) Stainless steel washer
e) Pipe fitting (3/8 inch) with drilled hole
f) Electrolyte collection container
g) Ultrasonic horn and convertor
h) Styrofoam disks
i) PVC Tee-joint
j) Fixture for mounting tool to Velmex system

A washer (d) was placed in one of the arms of the tee joint (i) and two Styrofoam disks (h) are placed as seen above. Finally, a pipe fitting (e) with a hole drilled into the center is used to close the arm of the tee joint and the ultrasonic probe tip is pushed

through this assembly. This ensured negligible back-pressure of electrolyte near (e). Any electrolyte flow towards (e) was collected in (f) and re-circulated back to the fresh electrolyte container. During experiments the ultrasonic probe tip (b) is vibrating at 40 kHz frequency and designated amplitude but there is no vibration near the Styrofoam disks (h). This is because the part of the ultrasonic probe near (h) is called the nodal area and the probe does not vibrate at nodes. Therefore, there are no concerns of unnecessary rubbing of probe with Styrofoam disks.

4. EXPERIMENTS

4.1 Design of experiment

A full factorial experiment was conducted based on four input parameters for exploratory investigation of ultrasonic amplitude and other process parameters (Table 2).

Variables	Levels
Ultrasonic Vibration Amplitude (%) – A_v	0, 15, 45
Peak Current (A) – I_p	22, 26
Pulsed Current Frequency (Hz) - f_c	0, 125, 275
Tool Feed Rate (µm/s) - f_r	10, 15

Table 2: Experimental Input Parameter

- Ultrasonic Vibration Amplitude

The ultrasonic vibration intensity is determined by the amplitude of vibration. Greater the maximum displacement of microtip, more intense the cavitation produced. The commercial ultrasonic probe used during experiments depicts amplitude values in the form of percentage. The use of a 3 mm diameter probe gives an amplitude range between 10 µm and 70 µm vibration. The micron value of amplitude at 10 µm, 40 µm and 70 µm is approximately 12 µm, 34 µm and 68 µm respectively. Other values can be approximately visualized from Figure 27. Two levels of ultrasonic vibration amplitude (A_v) selected were 15 µm and 36 µm. An additional level, where amplitude of vibration

was zero, was also added as a reference level. The selection of these values enabled to study the effect of high intensity cavitation of electrolyte on output parameters of ECM. Prolonged operation at very high amplitude (> 60 %) increased the chances of damage to ultrasonic probe and hence the "high" level was set at 36 µm. The low level was set 15 µm to observe difference between high and relatively low intensity cavitation.

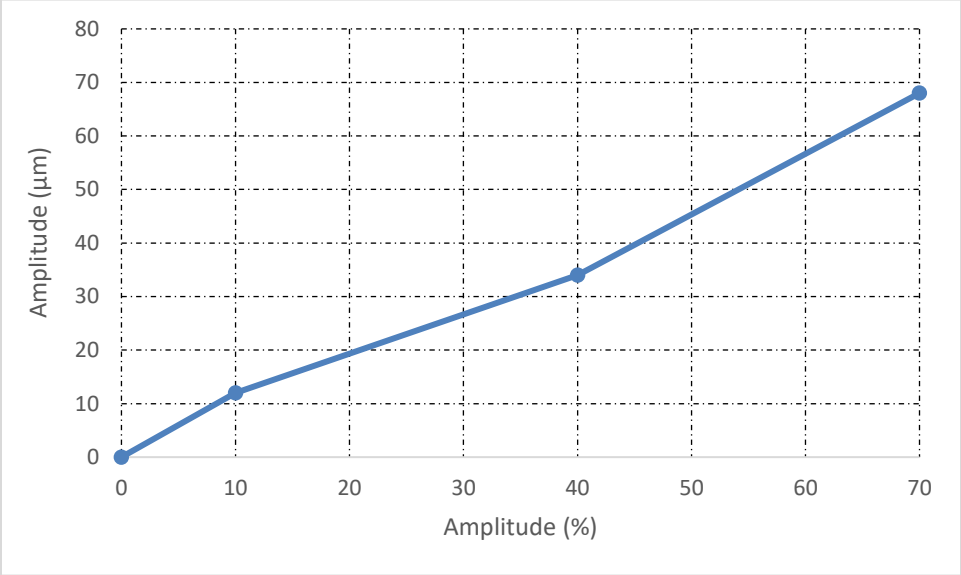

Figure 27: Approximate Values of Amplitudes in Micron In Term of Percentage Settings. Adapted from Corporation (2007)

- Peak Current

Two levels of peak current (I_p) were selected to further study the characteristics of laboratory ECM system. The current values selected were high to increase anodic dissolution rate. This would allow to observe if successful de-agglomeration of ECM by-products is achieved. These levels were selected after lower values of peak current result

in frequent contact between tool and workpiece. This happened because the constant travel speed of tool was faster than dissolution rate due to lower peak current.

- Pulsed Current Frequency

The power source used for experiments provided pulsed current frequency in the range of 0- 500 Hz for DC current. For this reason, two levels of pulsed current frequency (f_v) were selected at 125 Hz and 275 Hz to understand the benefits of more off-time during machining on output parameters. An additional level of zero pulsed current frequency (constant DC power) was added in the design in order to observe the absolute significance of pulsed current. This level also allowed to understand if ultrasonic vibration alone can improve flushing of ECM by-products without using a more sophisticated pulsed DC power supply.

- Feed rate

Feed rate (f_r) was a dominant factor in deciding size of IEG, since experiments were performed in an open loop system (No gap monitoring). Use of feed rates less than 10 µm would result in higher machining time, increase the IEG during machining and increase the effect of stray current. Use of very high feed rates, on the other hand would result in contact between tool and workpiece. For this reason, based on initial verification experiments, two levels of feed rate used in experiments were 10 µm/s and 15 µm/s.

Experiments were performed with direct current (0 Pulse Frequency) and without ultrasonic vibration for reference. Each experimental run was performed twice for repeatability. The experiments were performed in blocks, where each level of ultrasonic vibration acted as a block. The last block of three different experimental settings was performed at 0 Hz Pulse frequency (DC current). The experimental runs were not

randomized but the additional levels of ultrasonic vibration amplitude and current pulse frequency were run after the original full factorial experiment. This would ensure the lack of bias in experiments. The consistency of the experimental system was also ensured by monitoring current and voltage for every experimental run. Some typical current and voltage plots are shown below and Table 3 shows the order of experimental runs.

Each plot depicts repetition of the same operating conditions. For the first set of plots (Figure 28 and Figure 29), both voltage and current follow similar trend in terms of starting and ending voltage and nature of graphs. The same applies to the second set of plots (Figure 30 and Figure 31).

For an open loop system, there is no feedback to monitor gap conditions and adjust tool position during machining. In such a system, voltage and current plots can depict the nature of IEG throughout the machining cycle.

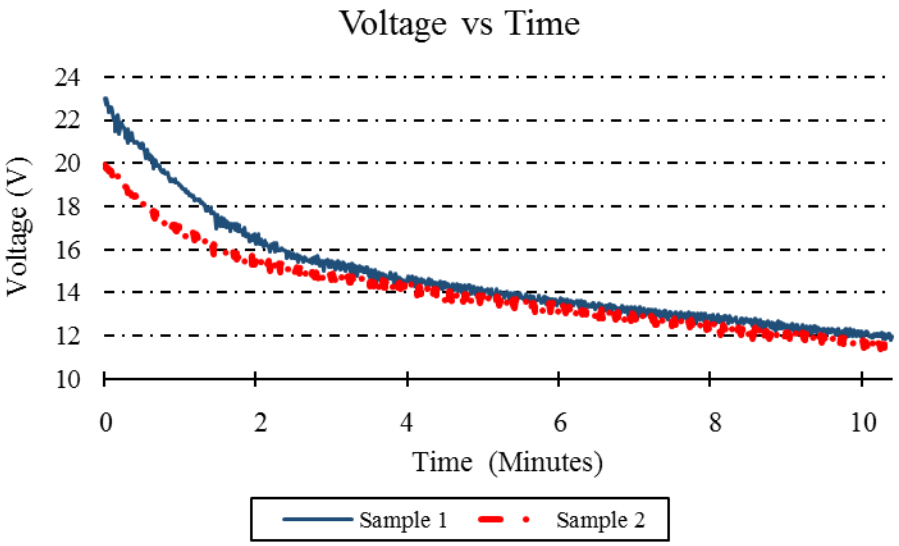

Figure 28: A Typical Voltage Vs Time Graph of Two Repetitions of The Same Operating Conditions: 15 µm A_v, 22 A I_p, 125 F_c, 10 F_r

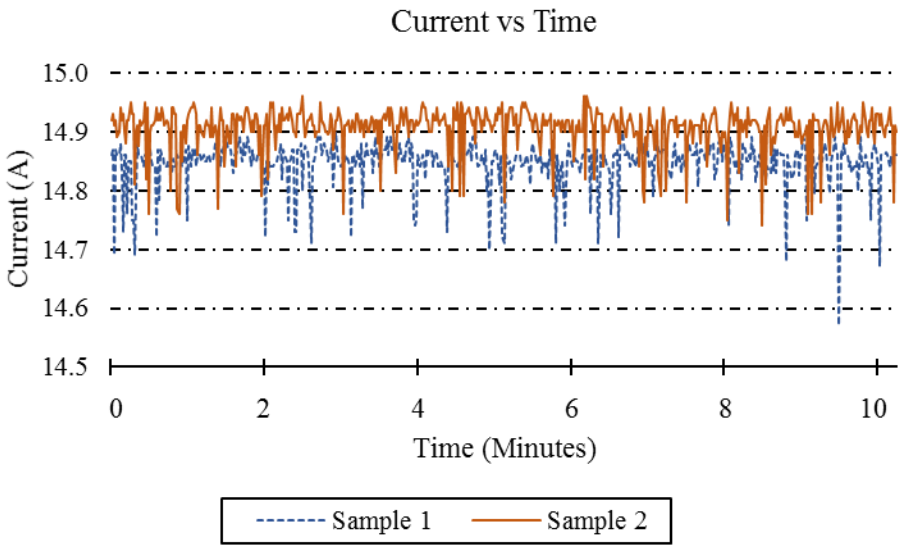

Figure 29: A Typical Current Vs Time Graph of Two Repetitions of The Same Operating Conditions: 15 µm A_v, 22 A I_p, 125 F_c, 10 F_r

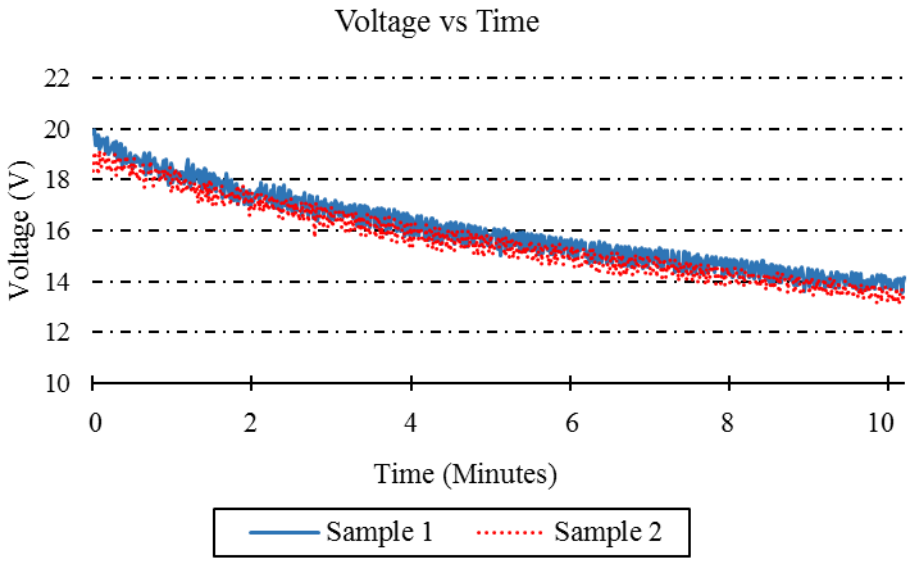

Figure 30: A Typical Voltage Vs Time Graph of Two Repetitions of The Same Operating Conditions: 15 µm A_v, 26 A I_p, 275 F_c, 10 F_r

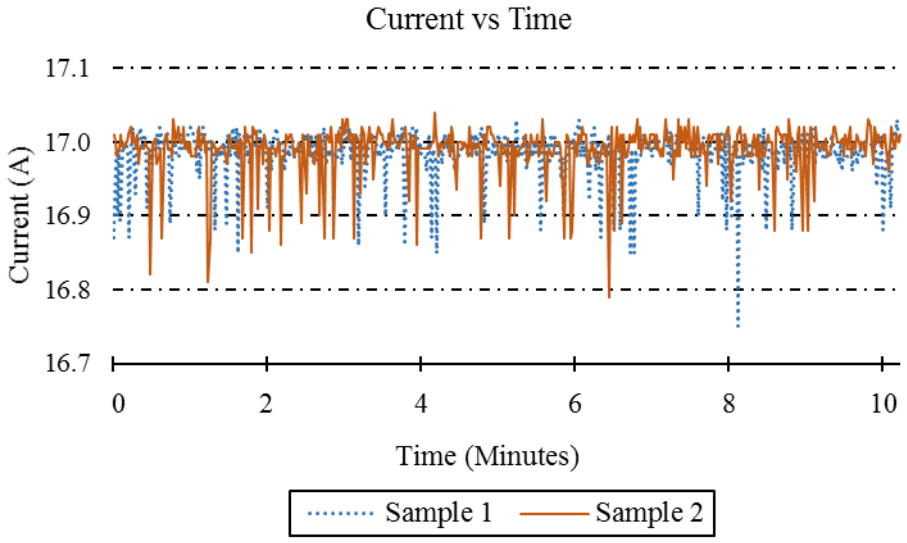

Figure 31: A Typical Current Vs Time Graph of Two Repetitions of The Same Operating Conditions: 15 µm A_v, 26 A I_p, 275 F_c, 10 F_r

The figure below shows the cross-sectional view of two ECM'ed holes machined at the same operating conditions. The picture further shows the repeatability of the laboratory ECM system.

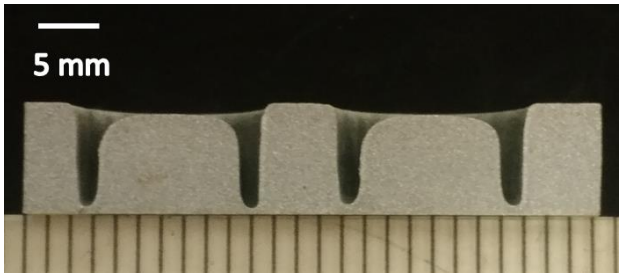

Figure 32: Section View by Wire- EDM of A Pair of Holes. Machining Conditions: 36 µm A_v, 22 A I_p, 275 F_c, 15 µm/Sec F_r.

Table 3 below shows the experimental runs at different design points on which experiments were performed.

Experimental Run No.	Ultrasonic Amplitude (%)	Peak Current (A)	Pulse Frequency (Hz)	Feed Rate (µm/s)
1	15	22	125	15
2			125	10
3			275	15
4			275	10
5		26	125	15
6			125	10
7			275	15
8			275	10
9	45	22	125	15
10			125	10
11			275	15
12			275	10
13		26	125	15
14			125	10
15			275	15
16			275	10
17	0	22	125	15
18			125	10
19			275	15
20			275	10
21		26	125	15
22			125	10
23			275	15
24			275	10
25	0	22	0	15
26	15			15
27	45			15

Table 3: Order of Experimental Runs

4.2 Experimental procedure

All experiments were conducted with Aluminum 6061-T6 as workpiece (60 mm long x 50mm wide x 6.3 mm thick). Holes were drilled with commercially teflon coated stainless steel tubes (Ø9.5mm OD, 0.3mm thickness). The length of the coated surface was 13 mm.

Potassium bromide (KBr) solution of concentration 1mol/L was used as electrolyte. Electrolyte was regularly filtered using settling method. The temperature of the electrolyte was measured before each experimental run using a Raytek Raynger ST infrared pyrometer. Each experimental run was started with electrolyte temperature in the range of 21-26 °C. Electrolyte conductivity was similarly measured before each run using the Hannah HI 8733 conductivity meter and was in the range of 111-121 mS/cm.

Before each experimental run, IEG was set using a digital multimeter and the Velmex positioning system as follows:

1. Workpiece and tool were secured and the Teflon coating from end of the tool was carefully grinded off to ensure conductivity.
2. The terminals of digital multimeter were connected to the cathode and anode wires of the machining system.
3. Tool was slowly brought into contact with the workpiece
4. Beeping sound of multimeter was an indication of contact between tool and workpiece and movement of tool was stopped.
5. Using COSMOS program 1 tool was moved exactly 0.3 mm away from the point of contact and thus initial IEG is set.

After setting the IEG, the desired input parameters required for the experimental run were set.

For running experiments, first the IEG is set at 0.3 mm. After turning on both pumps and ultrasonic vibration of probe, the power is switched on and immediately after that COSMOS program for tool to travel 6.2 mm at designated feed-rate is executed. After waiting for about 30 seconds from turning on power, voltage and current monitoring is turned on. The 30 second wait is in order to avoid initial surge which may damage the monitoring instruments.

Similarly, about 20 seconds before the end of the machining cycle, voltage and current monitoring is turned off. After travelling 6.2 mm perpendicularly into the workpiece, the tool is programmed to quickly withdraw away from the surface of the workpiece. Power supply, ultrasonic vibration and electrolyte flow is turned off immediately upon withdrawal of tool.

4.3 Measurement of output parameters

Alicona IFIF 3D profiler was used to measure the volume, surface roughness and taper angle of ECM'ed holes. This profiler generates 3D models of machined features based on the principle of focus variation.

After ECM, all samples were cleaned with water in an ultrasonic bath before being dried with compressed air. The samples were kept upside down to facilitate removal of dirt from the holes.

4.3.1 MRR measurement

4.3.1.1 Calibration of Alicona IF 3D profiler volume measurement:

In order to calculate the MRR of ECM'ed holes, volume was measured by scanning the holes using Alicona IF 3D profiler. In some samples, the scanning was not possible at every point on the surface of the hole. This is because the capture of reflected light is not possible at sidewalls as seen in Figure 33.

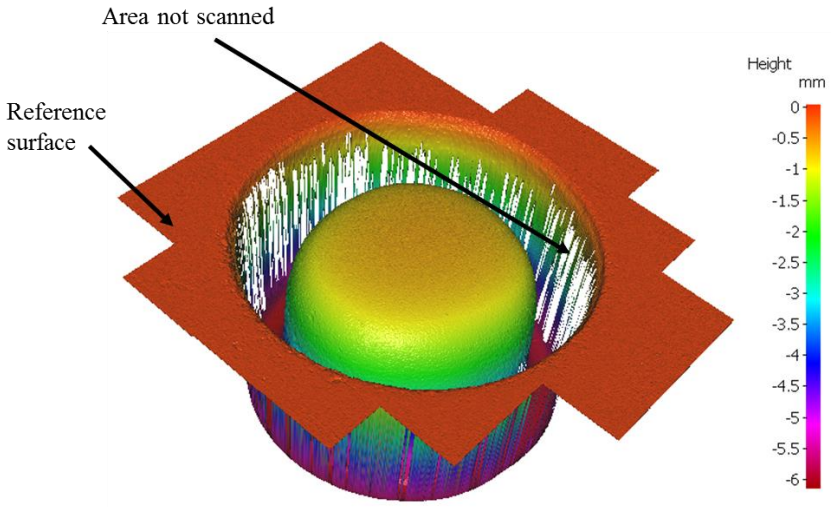

Figure 33: Typical 3D Model of Showing Regions in The Sidewall Not Scanned (Operating Conditions: 0 µm A_v, 26 A I_p , 275 Hz F_c , 15 µm/S F_r)

To verify the volume measurement module of 3D profiler, the volume of holes drilled at two different depths was calculated manually and compared with that obtained from the 3D profiler. The stepwise procedure is below:

1. 3 holes were drilled in a stainless steel plate. The circle measurement program of the Mitutoyo Vision System was used to measure the diameter of each hole. The program calculated the diameter based on the several data points selected along circumference of the hole. This step is illustrated in Figure 34.

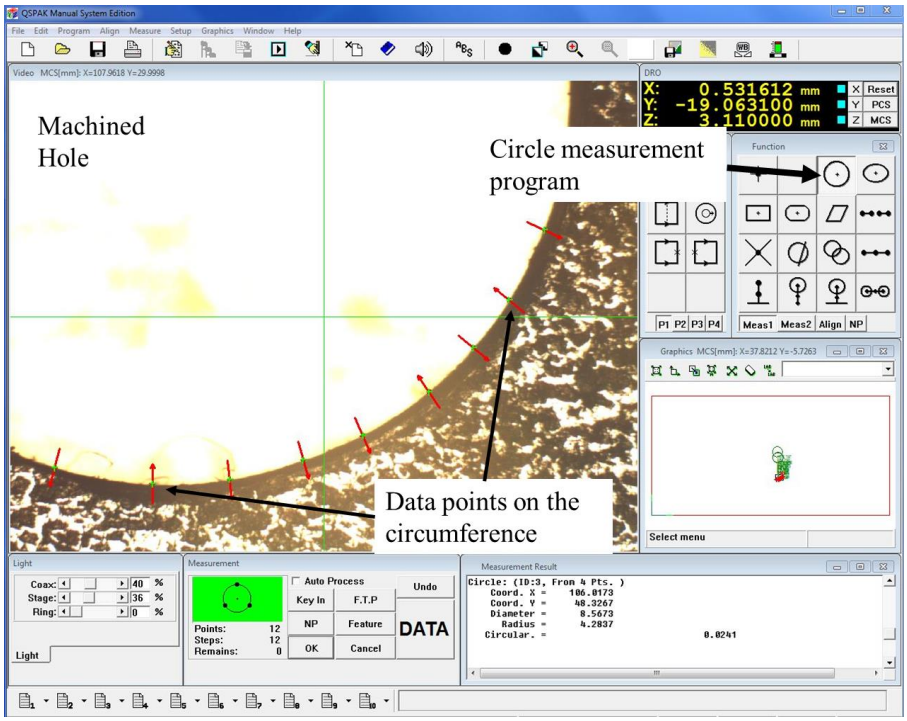

Figure 34: Calculating the Diameter of the Hole Using Mitutoyo Vision System

2. The thickness of the plate (i.e. depth of the hole) was measured using the vision system as well. The topmost surface of the plate was brought into focus first and then focus was changed to the bottom of the hole. The change in Z axis coordinates was noted and that was the depth of the hole. This step is shown in Figure 35.

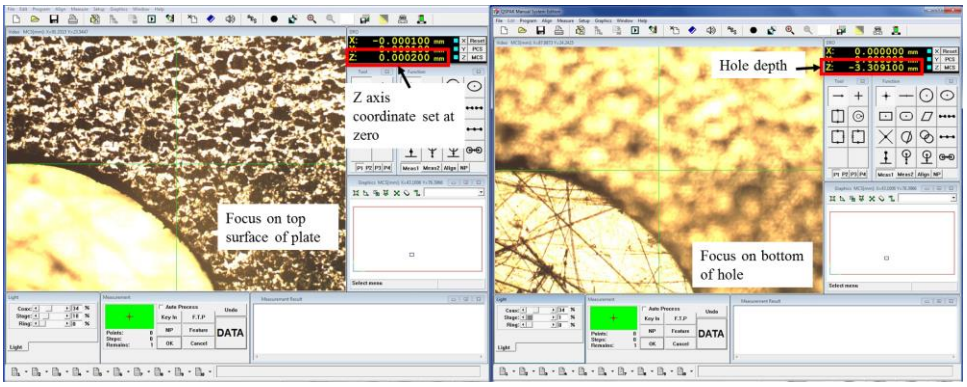

Figure 35: Measuring Hole Depth Using Vision System

3. 3D models of all the 3 holes were generated using Alicona IF 3D profiler as seen in Figure 36. These models were used to obtain volume using the volume measurement module of the profiler.

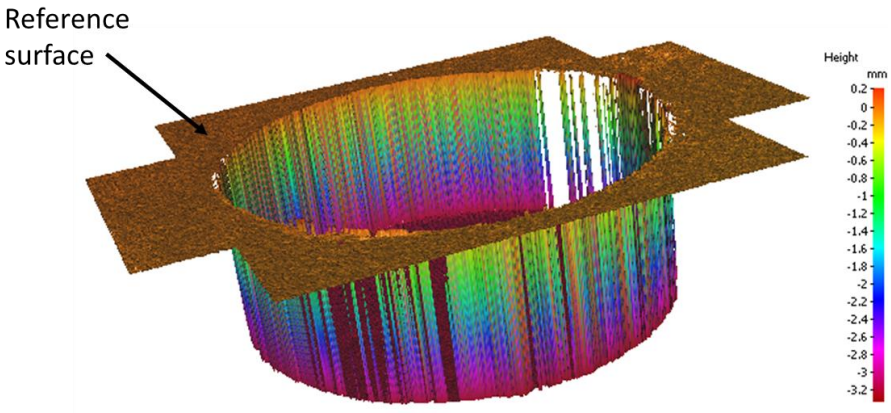

Figure 36: 3D Model of Typical Hole Drilled for Calibration

4. Finally, the volume of each hole was calculated based on the diameter and depth. These values were then compared with the volume measured using Alicona IF profiler for each hole.

4.3.1.2 Measurement of MRR of ECM'ed holes

MRR for the ECM'ed holes was measured using the volume measurement module of Alicona IF 3D profiler. The volume measured by the profiler was then divided by appropriate machining time to get MRR. Each experimental run was repeated once and therefore two different holes were obtained for the same experimental run.

The volume of the holes was measured twice for each experimental run. As seen in Figure 33 ,the generated 3D model enabled setting of a reference plane and the system calculated volume below the surface (i.e. the hole volume).

Below are the steps performed to obtain the volume of each ECM'ed hole:

1. A 3D model as seen in Figure 33 was obtained by scanning the entire area of the hole and focusing at the topmost surface and deepest part of the groove.
2. Volume measurement module was opened and the topmost surface was selected as the reference plane.
3. Volume measurement was selected and the 3D profiler automatically computed volume above and below the surface. Since the topmost surface was the reference plane, volume under the surface was the volume of the hole.

4.3.2 Surface finish measurement

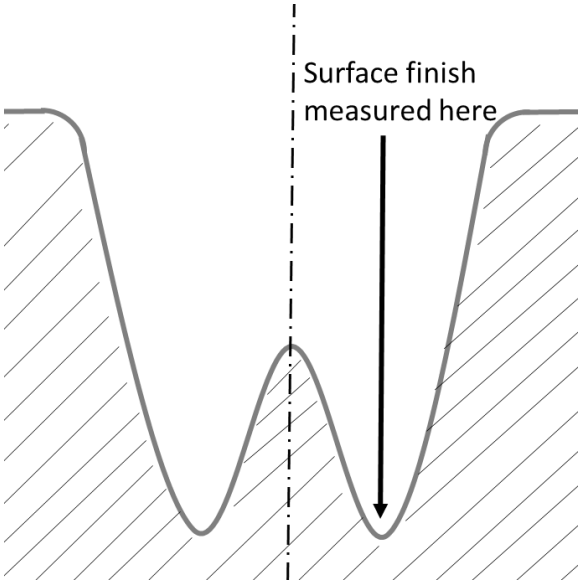

Figure 37: Surface Roughness Measurement Location

The line roughness module of the 3D profile was used to obtain surface roughness (R_a and R_z) measurements. 10 values of average surface roughness (R_a) at each experimental run and mean peak roughness (R_z) at selected design points were obtained in the following manner:

1. A small sample of surface was scanned in the groove of the ECM'ed hole as seen in Figure 37.
2. Line roughness measurement module was selected and a measurement on the sample was made. Measurements were made along the length of the groove

surface by drawing a 4 mm long profile and not across it to avoid measurement of waviness instead of roughness.

3. In order to complete 4 mm profile length profile was drawn in a zig-zag manner as seen in Figure 38. The zig zag profile line in the figure is over-highlighted for visibility.
4. 5 measurements were made on each sample and then this process was repeated for the second sample of the same set of experimental conditions, giving 10 values of average surface roughness (R_a). Figure 38 shows a snapshot of the line roughness measurement procedure.

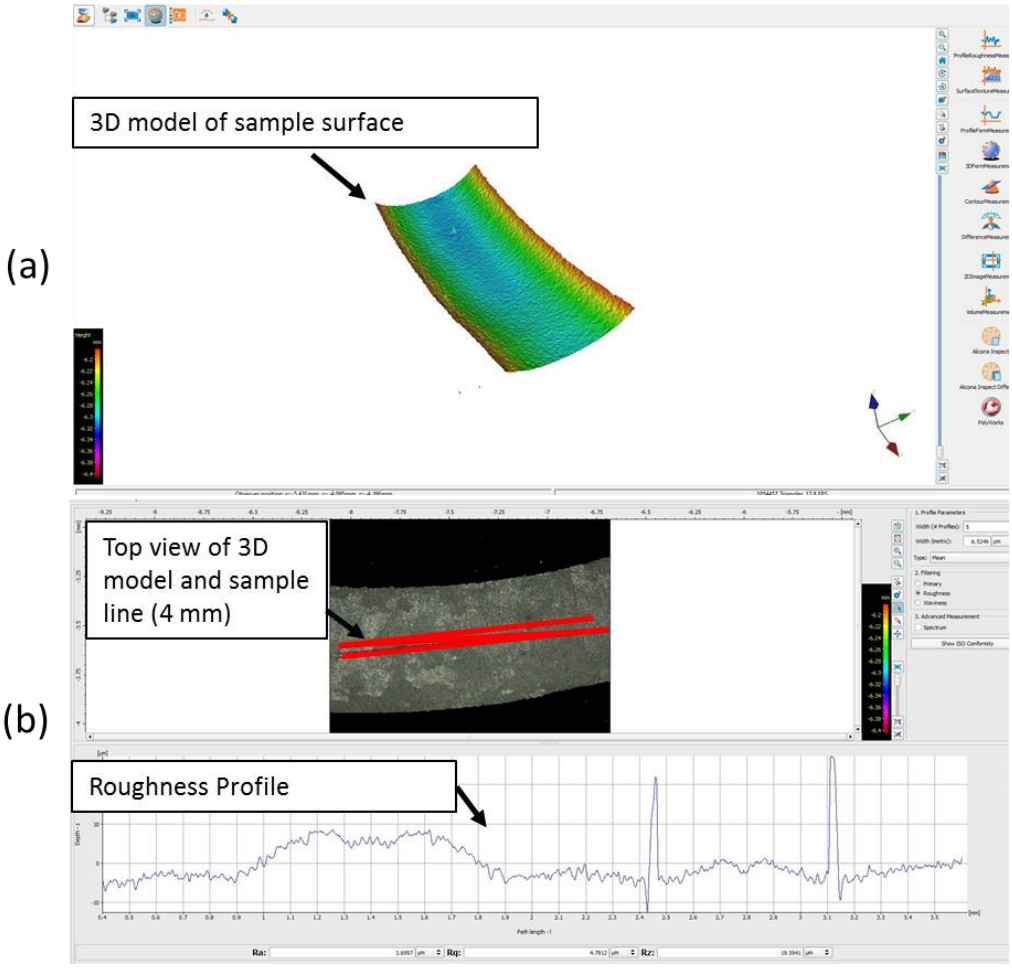

Figure 38: Line Measurement at the Bottom of the Hole. (a) 3D Model of the Sample Surface (b) Line Measurement Module Showing Top View of the Surface on which Sample Line is Drawn for Measurement

Typical measurements for average peak roughness (R_z) were also performed in a similar manner for all samples ECM'ed at 22 A I_p and 15 µm/s f_r.

The typical surface topography plot shown in Figure 49 is generated exporting the numerical data for individual roughness profiles and superimposing two appropriate different roughness profiles.

4.3.3 Taper angle measurement

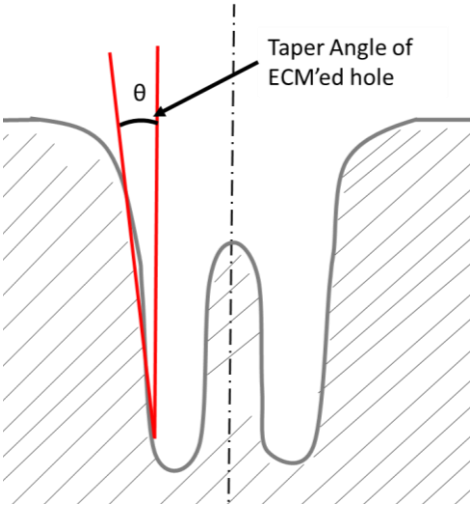

Figure 39: Definition of Wall Taper Angle in An ECM'ed Hole

Figure 39 illustrates taper in an ECM'ed hole and an approximate taper angle corresponding to it. This taper angle was measured for typical experimental conditions, namely all the samples ECM'ed at 22 A I_p and 15 µm/s f_r. The profile measurement module of the 3D profiler was used to measure taper angle in the following manner:

1. 3D model of ECM'ed hole was opened in the form measurement module of the Alicona IF profiler. The top view of the ECM'ed hole appears. A line is drawn across the groove of the hole to generate a sectional profile of the side wall of the hole. This step is illustrated in Figure 40 (a).
2. Next, data points are selected along 20 different points (maximum allowed by the system) along the hole sidewall. After registering these points, 20 more points

are selected along the vertical feed axis. Each click of the mouse registers a point. This step is illustrated in Figure 40 (b).

3. After data point selection, the form measurement module fits an angle through both the sets of points selected above and thus taper angle is obtained as seen in Figure 40 (c).

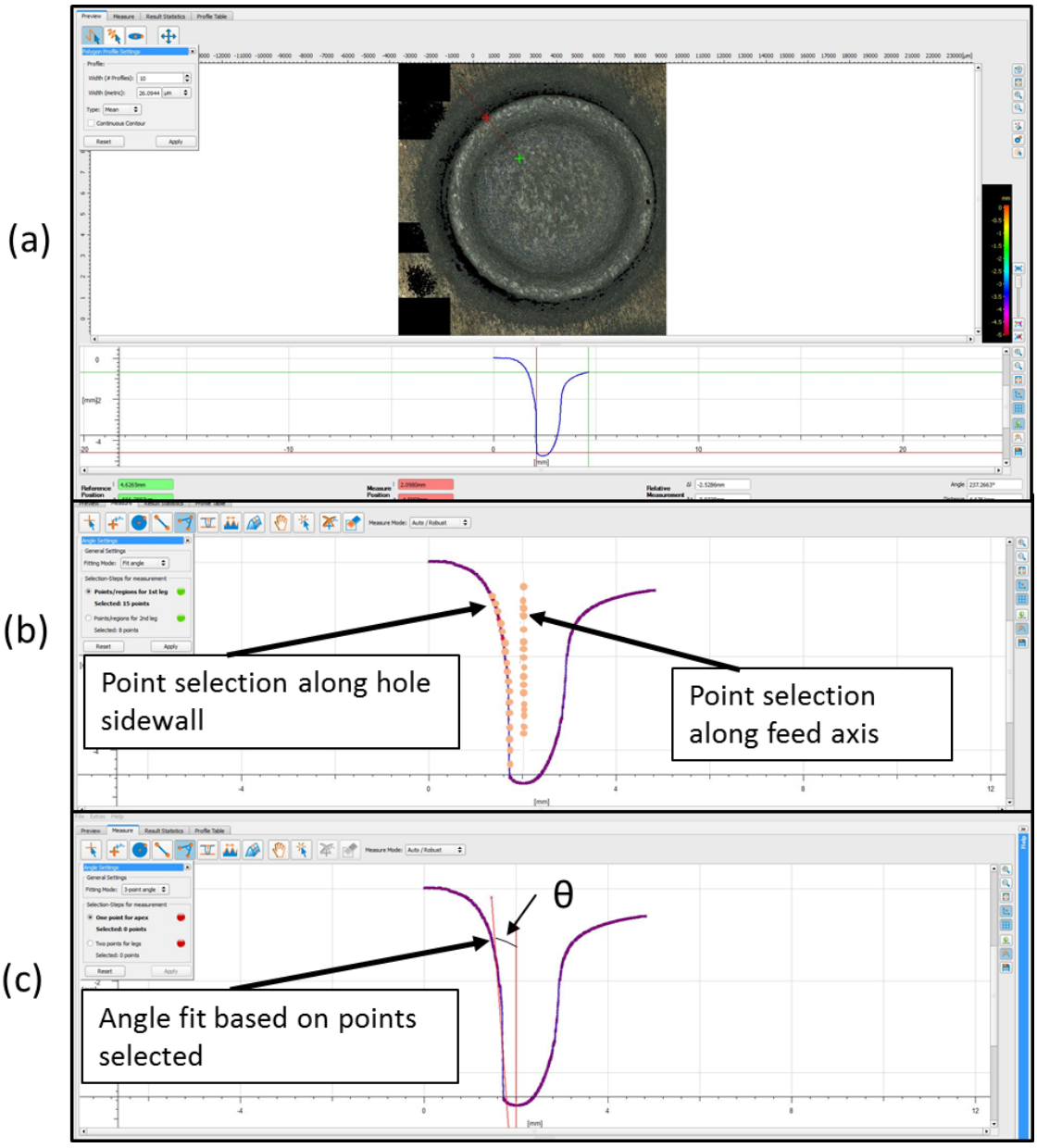

Figure 40: Taper Angle Measurement by 3D Profiler

After data was collected, Minitab Software was used to analyze data and observe the effects of relevant process parameters on MRR, Roughness parameters (R_a and R_z) and Taper angle of hole.

5. RESULTS AND DISCUSSION

This section discusses the effect of process parameters on MRR and hole quality, which includes profile roughness parameters (R_a and R_z) and taper angle of hole side wall.

Table 4 contains mean and standard deviation of output parameters measured. Complete experimental data are documented in Appendices C, D and E.

The ECM by-products mentioned and discussed in subsequent sections are formed as below:

5.1 ECM by-product formation

Workpiece material: Aluminum (Al)

Electrolyte material: Potassium Bromide (KBr)

The anodic dissolution of the workpiece generates Aluminum cations as shown below:

$$Al \rightarrow 3Al^{3+} + 3e^{-} \quad (2)$$

As for the aqueous solution of the electrolyte KBr, hydroxyl ions are formed from water and electrolysis of KBr occurs as follows:

$$H_2O + 2e^{-} \rightarrow H_2 + 2OH^{-} \quad (3)$$

$$KBr \rightarrow K^{+} + Br^{-} \quad (4)$$

The reactions above can be combined into one reaction:

$$Al + 3H_2O + KBr \rightarrow 2Al^{3+} + 3H_2 + 6OH^{-} + K^{+} + Br^{-} \quad (5)$$

Therefore, the ECM by-product formed during this study is either dialuminum hexabromide or the more stable aluminum bromide.

$$Al^{3+} + Br^{-} \rightarrow AlBr_3(\textbf{aluminum tribromide}) + Al_2Br_6(\textbf{dialuminum hexabromide}) \quad (6)$$

Amplitude (%)	Peak Current (A)	Pulse Frequency (Hz)	Feed Rate (µm/s)	MRR (mm^3/min)		Line Roughness-Ra (µm)		*Peak Roughness Rz (µm)		*Taper Angle (°)	
				Mean	Standard Deviation	Mean	Standard Deviation	Mean	Standard Deviation	Mean	Standard Deviation
15	22	125	15	21.99	0.26	1.41	0.25	3.67	0.91	1.68	1.76
	22	125	10	31.14	0.14	1.34	0.11	-	-	-	_
	22	275	15	33.28	0.36	1.07	0.17	3.13	0.95	0.69	0.48
	22	275	10	30.15	0.08	1.00	0.07	-	-	-	_
	26	125	15	28.73	0.77	0.90	0.12	-	-	-	_
	26	125	10	31.57	0.46	1.33	0.17	-	-	-	_
	26	275	15	31.37	0.84	0.85	0.12	-	-	-	_
	26	275	10	32.34	0.12	1.17	0.09	-	-	-	_
45	22	125	15	20.05	0.10	1.24	0.17	6.08	1.30	1.47	0.36
	22	125	10	28.69	0.36	1.47	0.26	-	-	-	_
	22	275	15	30.67	0.44	1.69	0.22	4.04	0.92	0.89	1.62
	22	275	10	29.70	0.09	1.84	0.31	-	-	-	_
	26	125	15	27.71	1.03	1.39	0.13	-	-	-	_
	26	125	10	30.84	0.11	2.40	0.66	-	-	-	_
	26	275	15	27.05	0.85	1.11	0.28	-	-		_
	26	275	10	30.84	0.15	2.46	0.73	-	-	-	_
0	22	125	15	29.21	0.36	2.16	0.42	9.81	0.97	2.71	0.55
	22	125	10	31.60	0.14	3.18	0.83	-	-	-	_
	22	275	15	33.54	0.20	2.53	0.79	12.28	2.79	2.31	0.39
	22	275	10	32.38	0.03	3.10	0.83	-	-	-	_
	26	125	15	34.53	0.01	2.91	0.93	-	-	-	_
	26	125	10	32.04	0.06	3.09	0.51	-	-	-	_
	26	275	15	37.82	0.15	2.75	0.77	-	-	-	-
	26	275	10	37.26	0.66	3.26	0.52	-	-	-	-
0	22	0	15	29.75	0.34	1.97	0.24	11.47	3.56	10.99	1.92
15				30.06	0.38	1.05	0.13	2.96	0.41	3.85	0.63
45				30.63	0.32	1.03	0.11	3.34	0.38	5.24	0.23

Table 4: Average MRR, Line Roughness and Taper Angle Measurements. * Taper Angle and R_z, were Measured Only for Samples ECM'ed at 22 A I_p and 15 µm/S f_r

5.2 Material Removal Rate

5.2.1 MRR measurement calibration

Below are the results from the calibration of the volume measurement as discussed in section 4.3.1.1. Table 5 shows the dimensions required to calculate volume of drilled holes. It also shows the theoretical volume V_1 and the volume measured by Alicona IF profiler V_2. The percentage difference between $V_{1 \text{ and }} V_2$ is negligible (< 1%).

Hole	Measured Hole depth (mm)	Measured diameter (mm)					Average Diameter (mm)	Average Theoretical Volume (mm^3)	Volume measured by Alicona Profiler (mm^3)	Percentage change between V_1 and V_2
		1	2	3	4	5		V_1	V_2	
1	3.30	8.45	8.46	8.44	8.42	8.42	8.44	184.53	185.55	0.55
2		8.56	8.48	8.43	8.51	8.41	8.48	186.26	185.06	-0.64
3		8.48	8.43	8.48	8.47	8.45	8.46	185.55	185.49	-0.03

Table 5: Calibration Results of Volume Measurement by Alicona IF Profiler

From above it can be seen that that there seems to be negligible influence of regions not scanned on the volume measurement by Alicona.

5.2.2 MRR results

MRR depends on the anodic dissolution reaction rate. According to Faraday's law, the material removed in unit time is proportional to the charge applied to the electrochemical cell. Therefore, an increase in the value of peak current results in a higher MRR (Figure 41).

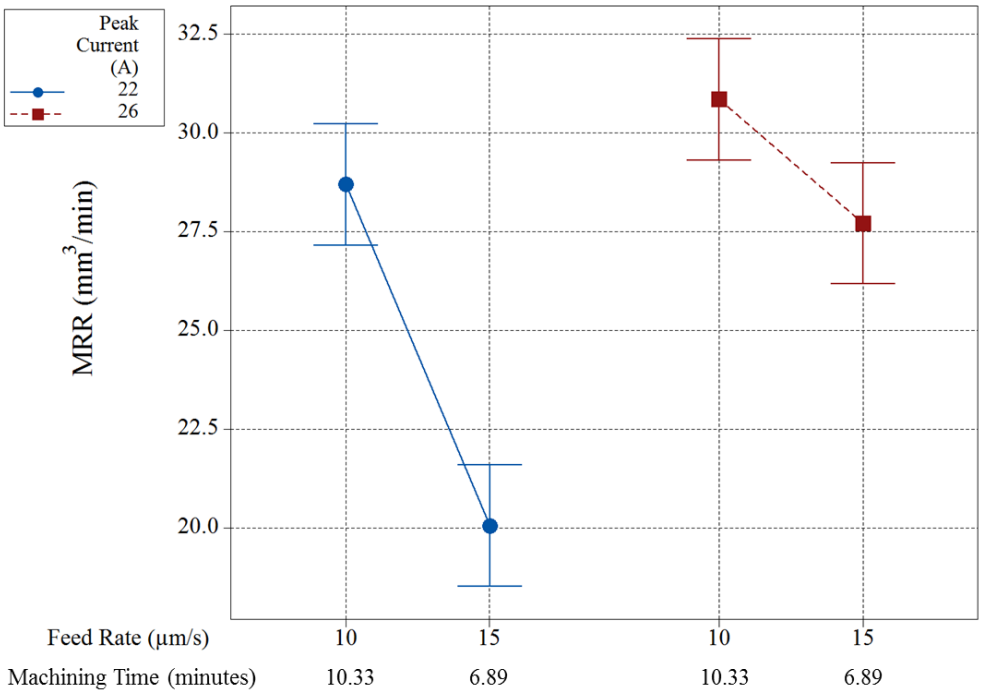

Figure 41: Effect of Peak Current and Feed Rate on MRR (Operating Conditions: 125 Hz F_c, 36 µm A_v). Interval Plot Is 95% Confidence Interval (CI) of the Mean.

From Figure 41 there is reduction in MRR with increasing feed rate. Since the travel distance of the tool is fixed (6.2 mm), a slower feed rate leads to more machining

time. This increases the time for stray current to increase overcut of the ECM'ed hole. Figure 42 illustrates the occurrence of overcut during ECM. Therefore, a slower feed rate i.e. longer machining time results in higher MRR. This factor becomes especially significant with the depth of the hole is higher. The effect of overcut can be seen in the section view of the hole groove in Figure 43.

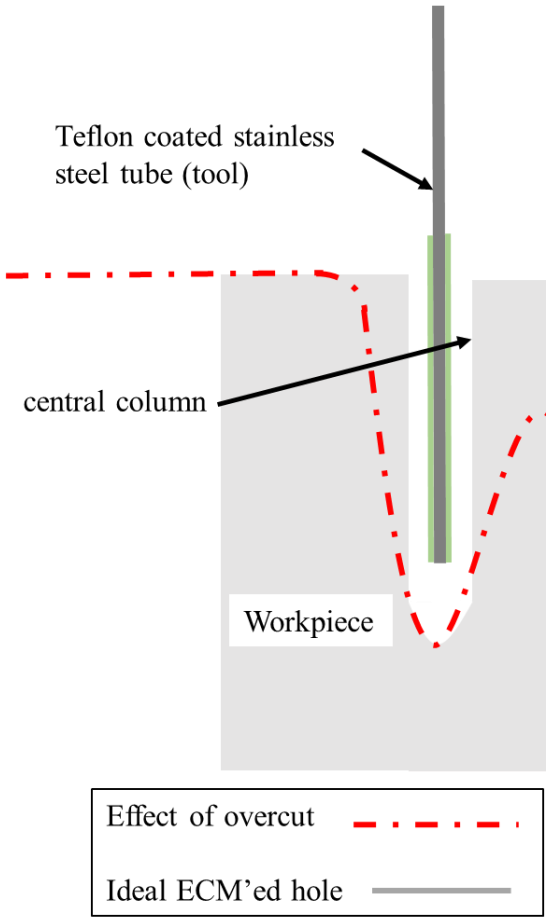

Figure 42: Illustration of Overcut In ECM

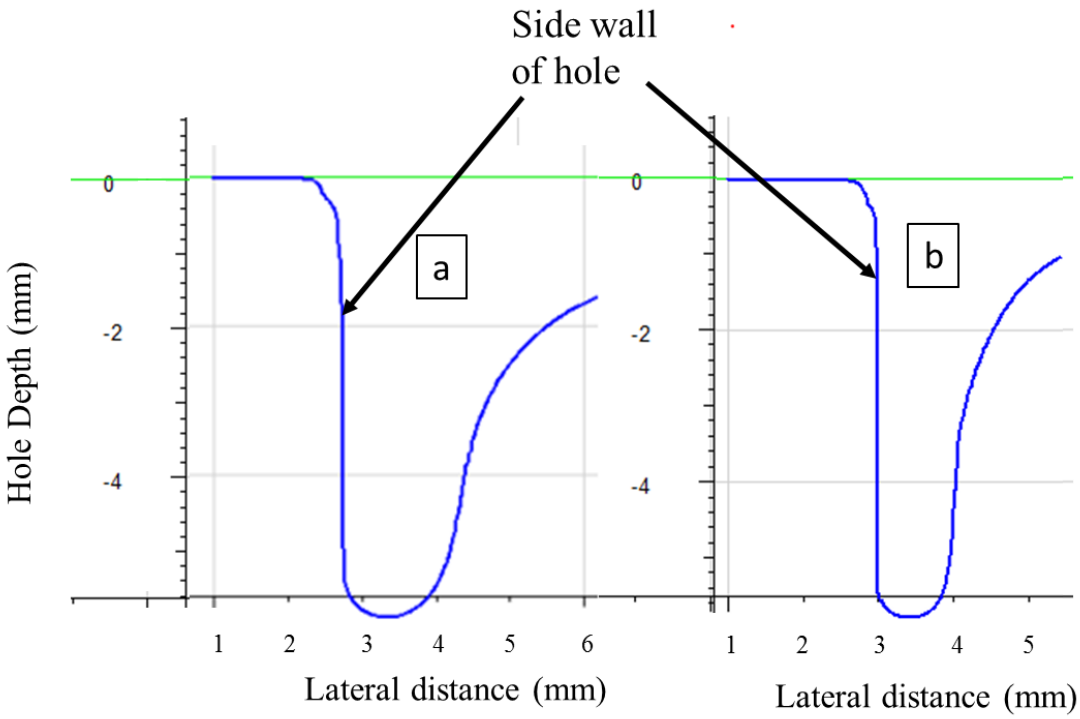

Figure 43: Comparison of Hole Groove At (A) Low (10 µm/S) and (B) High (15 µm/S) Feed Rates (Operating Conditions: 0 µm A_v 22 A I_p, 125 Hz F_c)

Figure 44 shows the effect of pulse frequency and ultrasonic vibration on MRR at 22 A I_p and 15 µm/s f_r. At 0 Hz pulse frequency, there is insignificant change in MRR as ultrasonic vibration amplitude increases.

With the application of pulsed current, the MRR at 125 Hz pulsed current frequency without any ultrasonic vibration is the same as MRR at 0 Hz. This indicates that the off time in machining at 125 Hz is not significantly influencing MRR yet. MRR significantly increases at 275 Hz and no ultrasonic vibration. This is due to the off time in machining that allows for ECM by-products to flush out of the IEG promoting stable

anodic dissolution. The use of pulsed DC current also reduces overheating and possible evaporation of electrolyte at the IEG. This promotes stable gap conditions and may contribute to improvement of MRR.

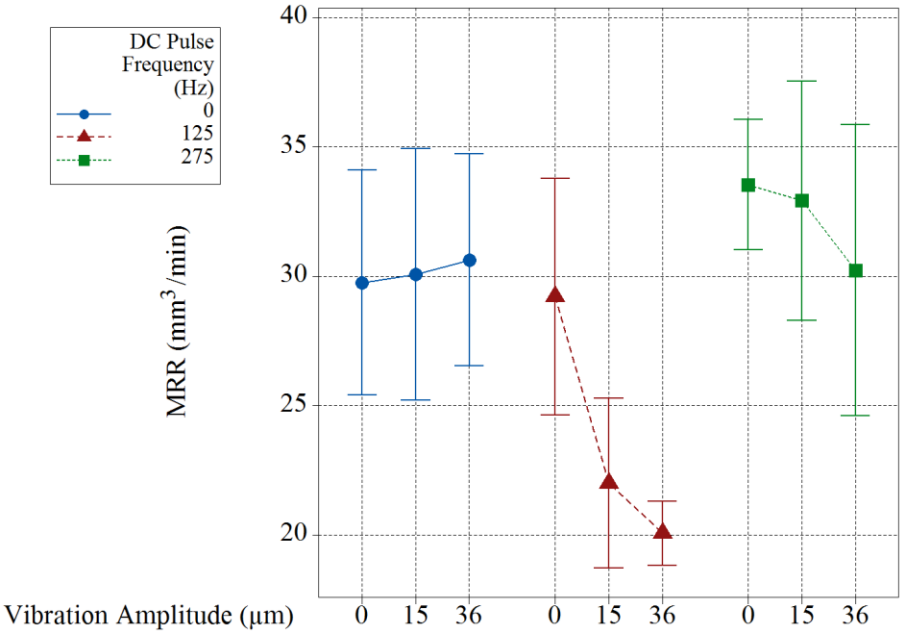

Figure 44: Effect of DC Pulse Frequency and Ultrasonic Vibration on MRR (Operating Conditions: 22A I_p, 15 µm/S F_r). Interval Plot Is 95% CI of The Mean.

Lastly, the combined effect of pulsed current and ultrasonic vibration seems to have a negative effect on MRR. The reason for that maybe the very high ultrasonic vibration amplitudes causing excessive cavitation in the electrolyte during, which results in reduction in rate of anodic dissolution during the on-time cycle of machining. Bubble formation due to intense cavitation results in periodic blocking of current between electrodes (Ryu, 2015). The bursting of cavitation bubbles increases the local pressure in IEG and suppresses the ionization process at the anode. This may slow down the ion

transport rate resulting in smaller MRR. Such results of reduction in MRR at high amplitude ultrasonic have been observed by other researchers. Wang et al. (2016) observed reduction of MRR during ultrasonic vibration of disk shaped tool at amplitude 11 µm vibration amplitude and frequency of 28 kHz.

Based on the data in Table 4, a linear regression equation for MRR can developed as below:

$$\boldsymbol{MRR = 14.72 - 0.2317\,A_v + 0.699\,I_p + 0.02277\,f_c - 0.201\,f_r} \qquad \textbf{(7)}$$

If feed-rate is replaced by machining time the following equivalent model is applicable

$$\boldsymbol{MRR = 9.71 - 0.2317\,A_v + 0.699\,I_p + 0.02277\,f_c - 0.292\,t_m} \qquad \textbf{(8)}$$

Where,

MRR	:	Material Removal Rate (mm^3/min)
A_v	:	Amplitude of vibration (0,15 µm)
I_p	:	Peak current (22,26 A)
f_c	:	Pulsed current frequency (125,275 Hz)
f_r	:	Feed rate (10,15 µm/s) for fixed drilling depth (6.2 mm)
t_m	:	Machining time (10.33 minutes at 10 µm/s, 6.89 minutes at 15 µm/s)

The coefficients of this model are applicable to input parameter values in the range specified above only. The R^2 value of this linear model is 66.78%. The residual plots below indicate the goodness-of-fit of the model. Since feed-rate and machining

time are equivalent factors, the residual plots of both the models above remain the same. The histogram plot roughly represents a bell curve, indicating that the residuals are normally distributed. There is no notable pattern in the residual versus fitted values and observation plots. This indicates that for the given factorial levels, the regression model captures majority of explanatory information.

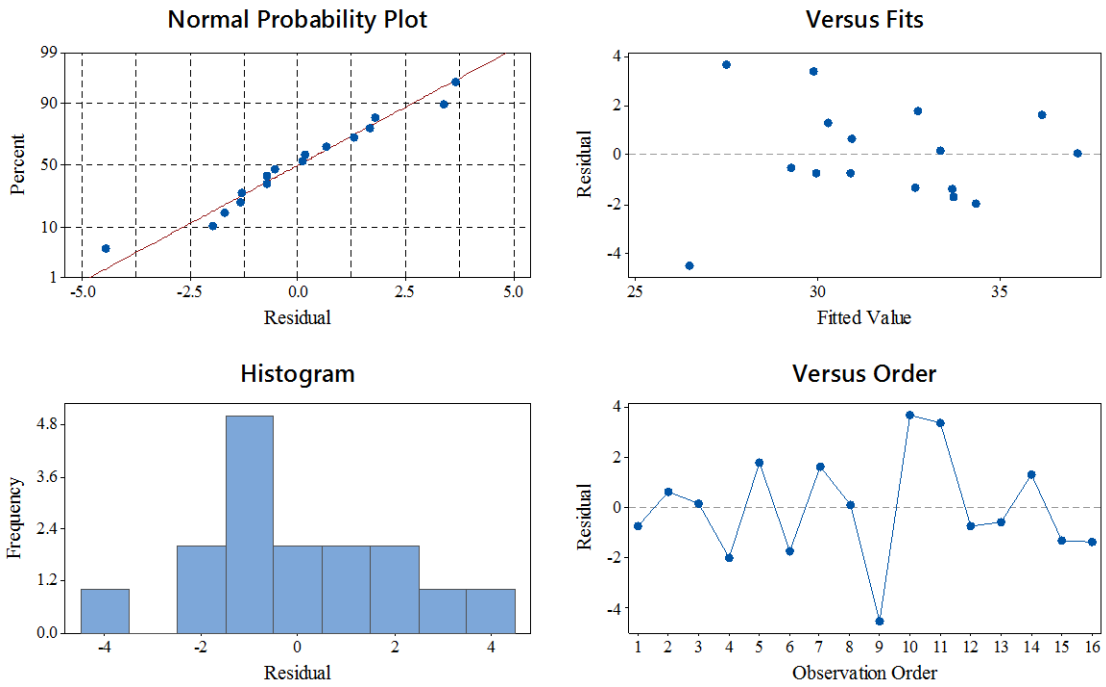

Figure 45: Residual Plots for Linear Regression Model of MRR

5.3 Profile Roughness

As already illustrated in Figure 42 and discussed in previous section, deep holes ECM'ed at slow feed rate result in a lot of stray machining. According to Serway et al. (2013), the voltage distribution during ECM of a plate with a hollow coated tube will be as seen in Figure 46. It is clear from below that the electrical field is strongest at the central column and exactly below the hollow tube. Due to this, the column in the center of the ECM'ed hole is more significantly machined by stray current during experiments performed low feed. All the ECM by-products generated by machining of the central column need to be flushed out of the IEG during experiments. At low feed rate, this debris interferes with the machining of the hole and that may cause non- uniform machining in the IEG. It is due to these effects that a better surface finish was seen at higher feed rates (Figure 47).

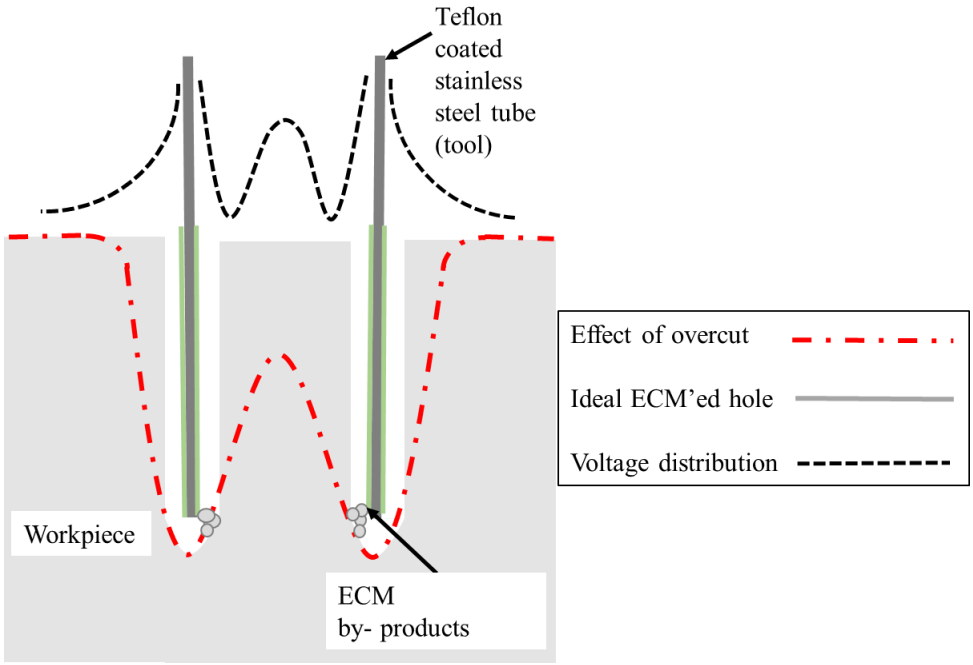

Figure 46: Effect of Stray Current and Voltage Distribution during ECM.

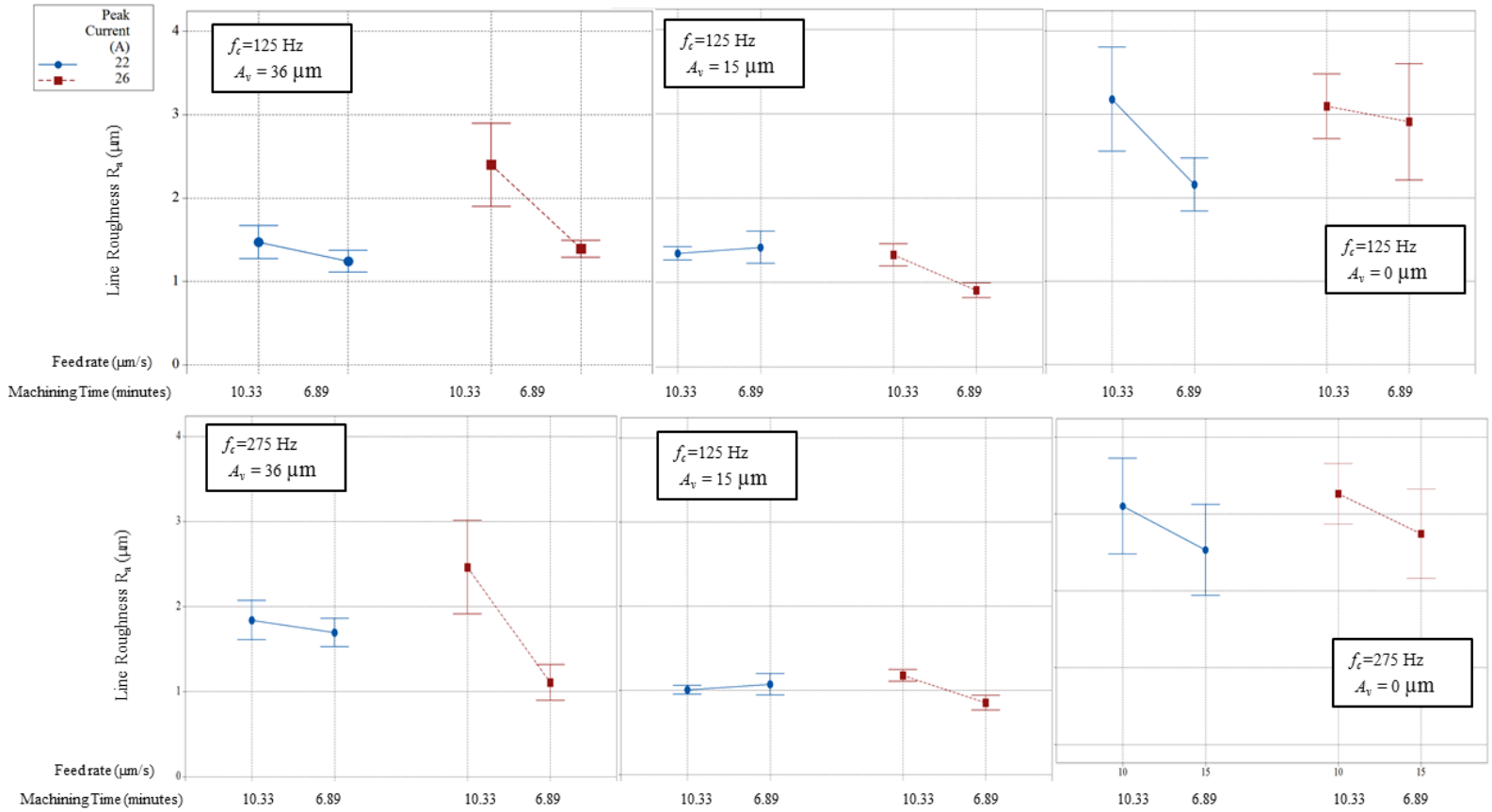

Figure 47: Effect of Feed Rate at Different Levels of F_c and A_v. Interval Plots Are 95% CI of The Mean.

Figure 47 and Figure 48 also show the effect of ultrasonic vibration amplitude on surface roughness. It can be seen from Figure 47 that the best surface finish is achieved at 15 µm ultrasonic vibration amplitude and 26 A peak current. This may be because the rate of dissolution at 26 A I_p and the rate of flushing at 15 µm A_v result in uniform machining in the IEG, giving a smoother surface.

As seen in Figure 48, pulsed current frequency without ultrasonic vibration increases surface roughness somewhat. The increase in MRR due to pulsed current maybe the reason behind the rougher surface. However, the best surface finish is obtained when 275 Hz f_c is applied along with 15 µm A_v. It is worth noting that better surface finish is also realized without the use of pulsed current at 15 µm and 36 µm A_v.

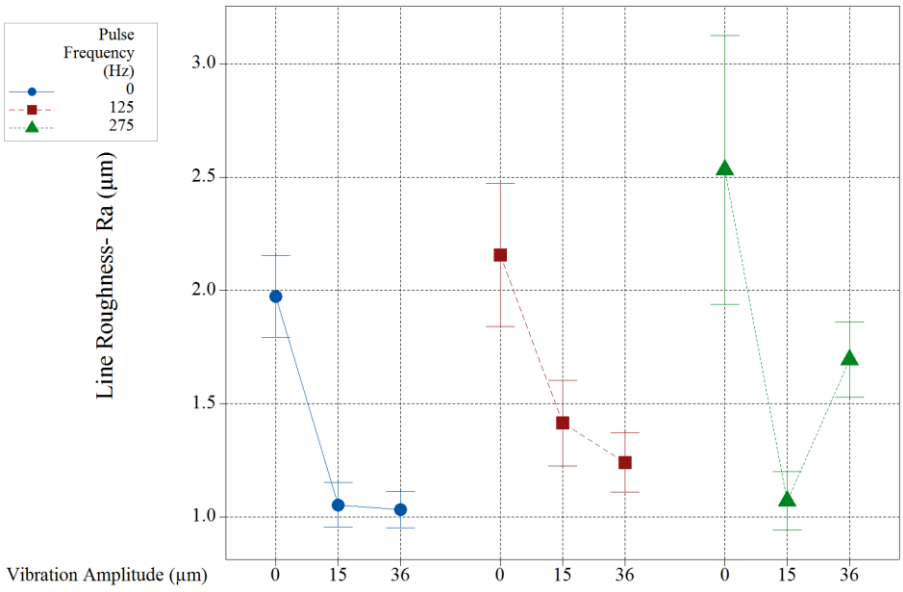

Figure 48: Effect of DC Pulse Frequency and Ultrasonic Vibration Amplitude on Average Line Roughness (Ra) (Operating Conditions: 22A I_p, 15 µm/S F_r). Interval Plot Is 95% CI of The Mean.

De-passivation of passive films, prevention of salt deposition and de-agglomeration of ECM by-products are thought to have contributed in surface finish improvement as discussed below.

- De-passivation

The prevention of formation of passivation layers is said to enhance the surface quality of ECM'ed feature (Ruszaj et al., 2007). There has been evidence of passivation layer formation, which may be several nanometers thick, for most metals in the form of non-conducting oxide (McGeough, 1974). It is present on most metals and there is evidence of its formation on aluminum as well (Racicot et al., 1996; Tak et al., 1994). The reduction in R_a and subsequent smoothening of profile can be attributed to reduction in passivation of anode surface. The formation of passivation layer results in non-uniform current density throughout the anode surface (Mitchell-Smith et al., 2016). This causes anodic dissolution to be at different rates at different points in the IEG during machining, resulting in a rougher surface finish. However, the continuous rupturing of such dissolution inhibiting layers creates uniform conditions for machining giving a smoother surface. Similar results were obtained by Mitchell-Smith et al. (2016) as previously seen in Figure 21.

- De-agglomeration of ECM by-products

The intense ultrasonic vibration prohibits deposition of salt layers on anode surface and constantly de-agglomerates debris particles to produce smoother surface.

Surface smoothening also may occur due to collapse of cavitation bubbles and microscopic roughening of surface (Ryu, 2015; Wang et al., 2016).

Figure 49 illustrates 2 typical roughness profiles where ultrasonic vibration results in smoothening of ECM'ed surface by reducing the peak roughness. All other operating conditions are constant and the sample length is the same (4 mm) for both the profiles below. The sample lengths were randomly taken at similar locations in each of the ECM'ed sample (as seen in Figure 37).

As seen below, application of 15 µm ultrasonic vibration amplitude reduces the peak roughness from over 15 µm to about 5 µm resulting in a decrease in the R_a value (from about 2.5 µm to 1.2 µm).

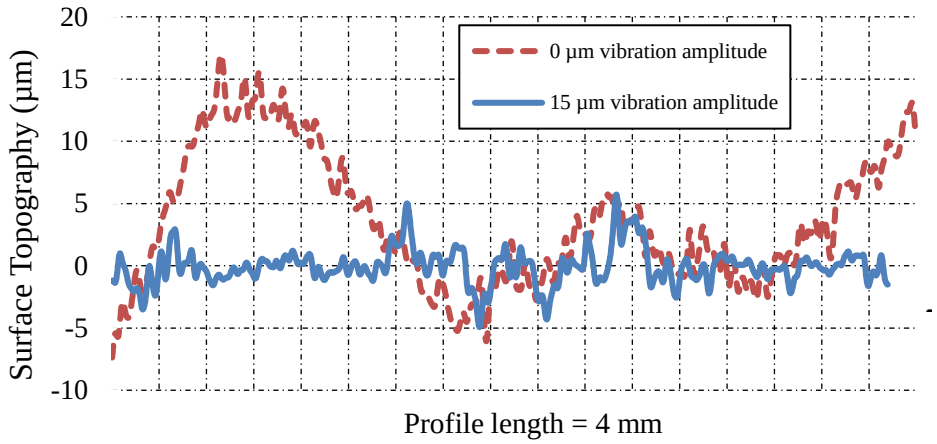

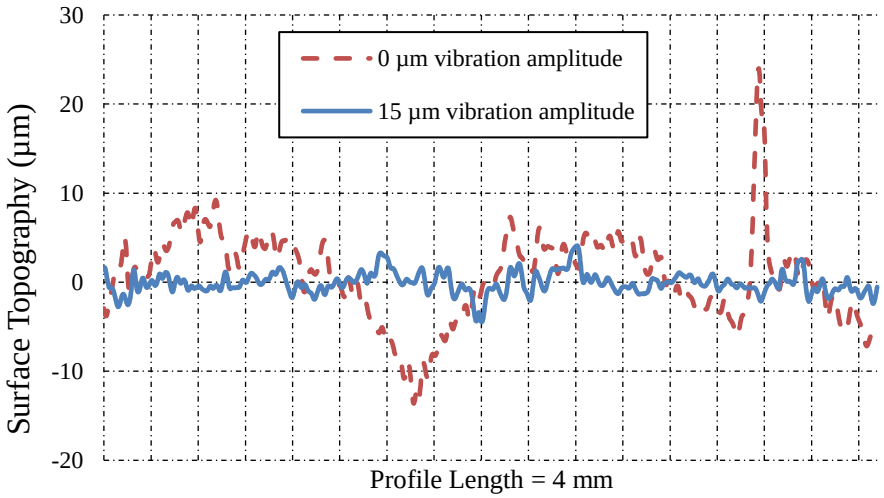

Figure 49: 2 Typical Surface Topography Samples (Operating Conditions: F_c = 275Hz, Ip=22A, F_r=15 µm/S).

The mean peak roughness value plot below shows reduced value of R_z for instances where ultrasonic vibration is used. The collapse of microscopic bubbles near the anode surface suppresses ionization (reducing MRR) while breaking up agglomerated ECM by-products on anodic surface. This reduced R_z values contribute to overall roughness reduction. The slight increase in roughness at 36 µm ultrasonic vibration amplitude indicates that highly intense cavitation is detrimental to surface finish of ECM'ed hole. Highly intense cavitation bubbles collapsing on the surface of the anode cause micro-pitting and therefore increase the surface roughness.

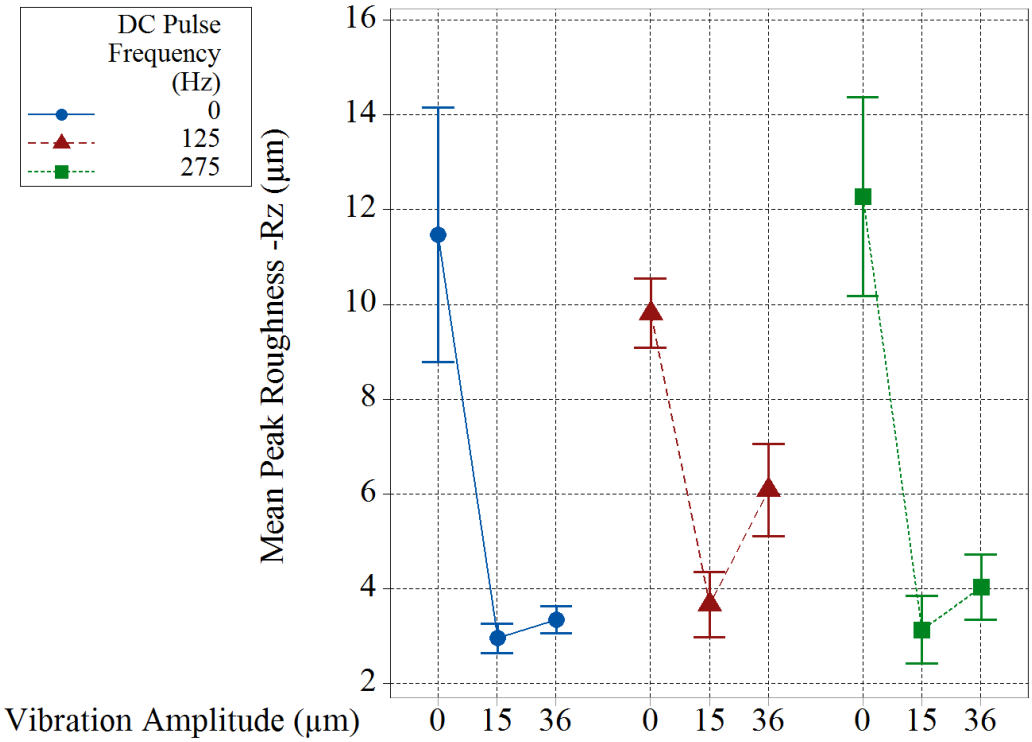

Figure 50: Effect of DC Pulse Frequency and Ultrasonic Vibration Amplitude on Average Peak Roughness (Rz) (Operating Conditions: 22 A I_p, 15 µm/S F_r). Interval Plot Is 95% CI of The Mean.

Using the data from Table 4, a simple linear regression model of Line Roughness (R_a) with main effects of input parameters was obtained as follows:

$$\boldsymbol{Ra = 3.519 - 0.11579 * A_v + 0.0148 * I_p - 0.0724 * f_r - 0.000482 * f_c} \quad \textbf{(9)}$$

Where,

R_a	:	Average line surface roughness (µm)
A_v	:	Amplitude of vibration (0,15 µm)
I_p	:	Peak Current (22,26 A)

f_c : Pulsed current frequency (125,275 Hz)

f_r : Feed rate (10,15 µm/s)

The R^2 value of this linear model is 94.41%. The coefficients of this model are applicable to input parameter values in the range specified above only. The residual plots below indicate goodness-of-fit of the model. The histogram plot of residuals roughly represents a bell curve indicating that the residuals. There is no clear pattern observed in the plots for residuals vs fitted value and observation order. This indicates sufficiently unbiased estimation of model coefficients.

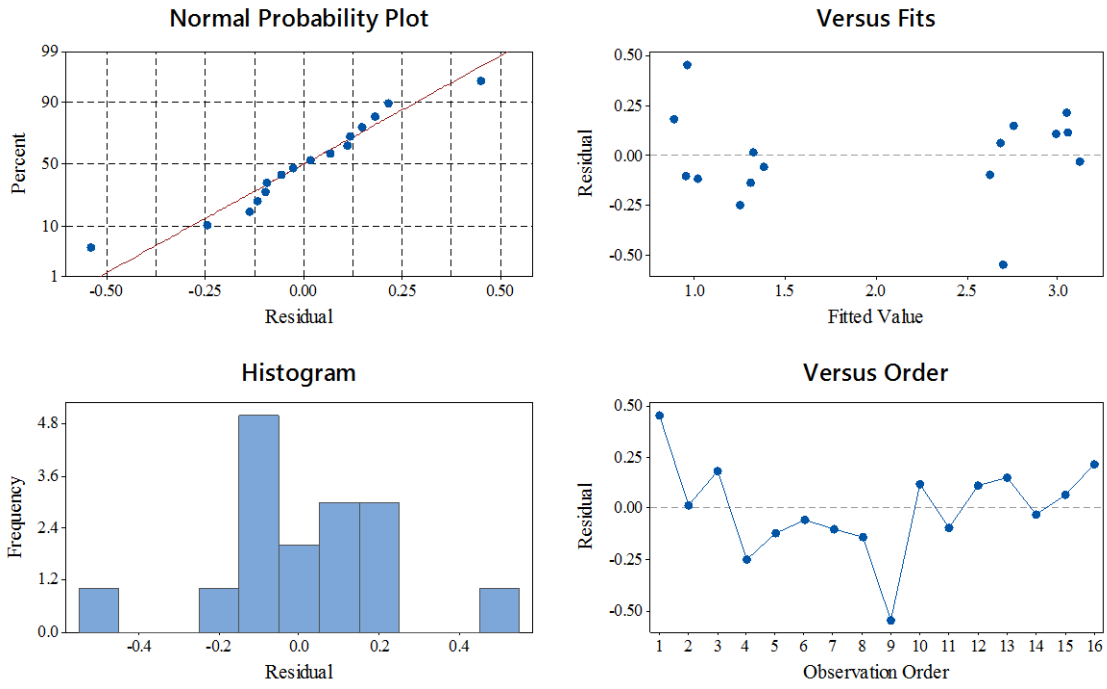

Figure 51: Residual Plots for Linear Regression Model of Line Surface Roughness (R_a)

5.4 Hole Taper Angle

Recall that the horizontal tubular electrode is used in machining of holes in this study. Hole taper was measured at the "12'o'clock" position of the hole, or the top part of the hole. This is because at the lower part of the hole ("6'o'clock" position) there is evidence of erosion (Figure 52). This erosion occurs due to fast flowing electrolyte throughout the machining cycle under the influence of gravity.

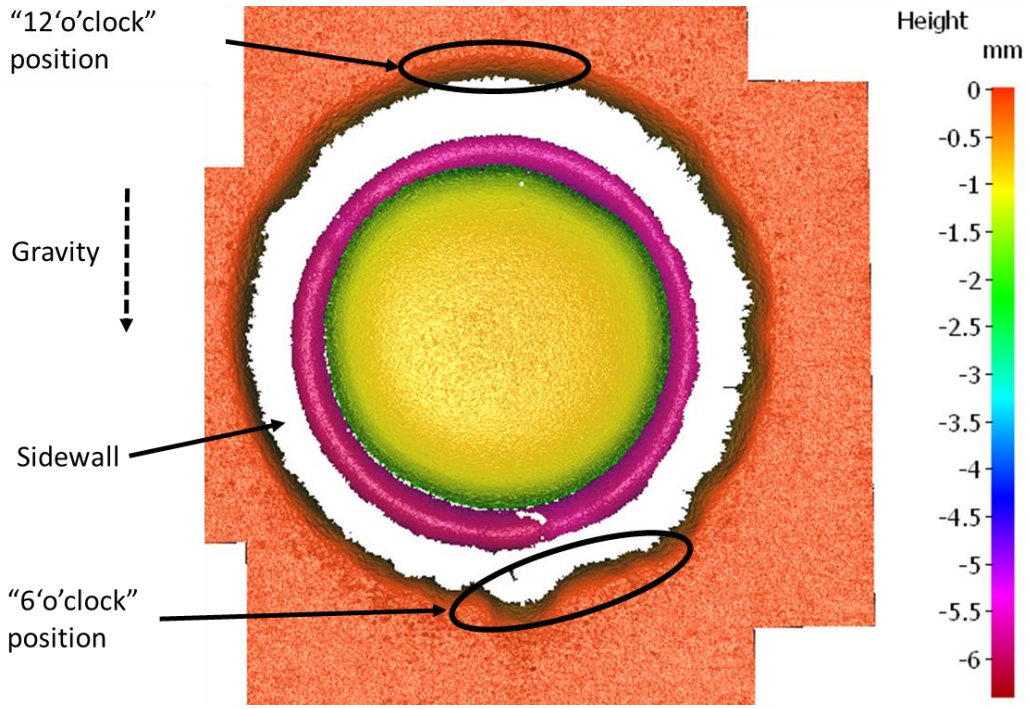

Figure 52: Illustrating Erosion Areas in ECM'ed Hole At "6 'O' Clock" Position

The passivation layers in the part of the anode directly intersecting with tool face force a change in the current density profile of the machined feature. Hence, it is

believed that such a phenomenon during deep drilling reduces removal in the direction of the feed and promotes geometrical inaccuracy in the form of taper of hole walls. The agglomerated ECM by-products may also erode the side walls while being flushed out of the IEG.

The results in Figure 53 show that without pulsed current the taper angle is the highest, proving the effect of pulse off time in improvement of geometric accuracy. However, the addition of ultrasonic vibration further reduces the taper angle, such that the combined effect of pulsed current at 275 Hz and 15-36 µm ultrasonic vibration amplitude brings the taper angle very close to 1°. Ultrasonic vibrations in fast flowing vibration breaks down machining products and hence makes removal of the debris easier from the deep hole and narrow side gaps.

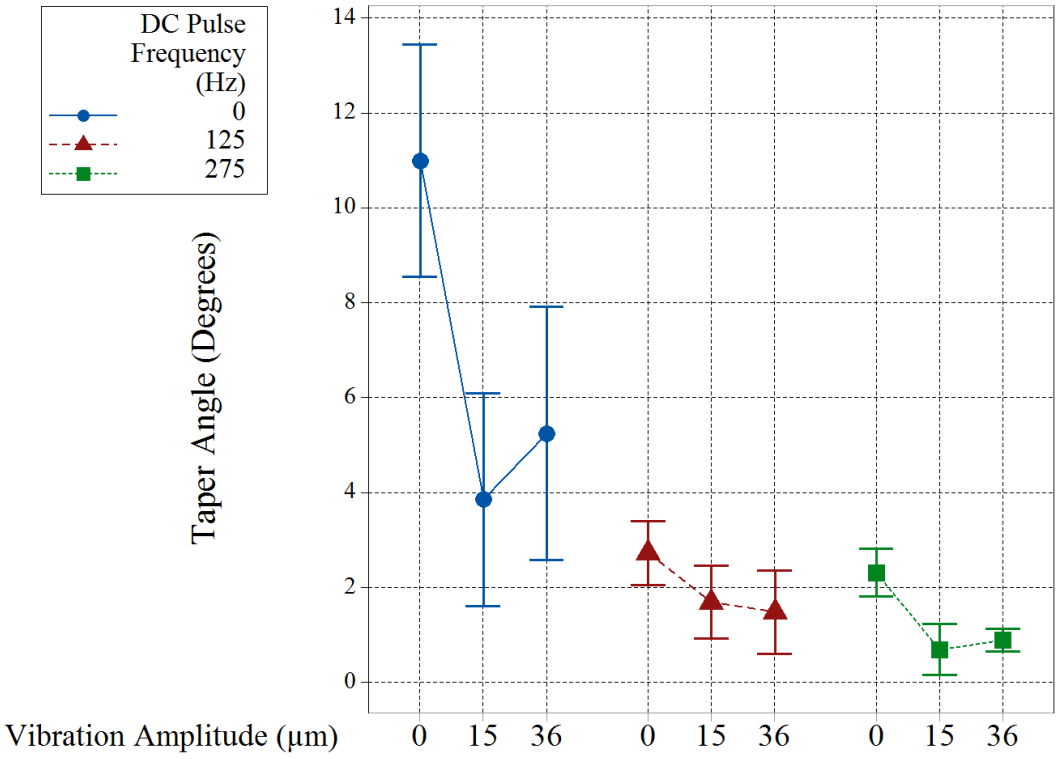

Figure 53: Effect of DC Pulse Frequency and Ultrasonic Vibration Amplitude on Taper Angle of Hole (Operating Conditions: 22A I_p, 15µm/S F_r). Interval Plot Is 95% CI of The Mean.

6. CONCLUSION AND RECOMMENDATIONS

A novel technique of applying ultrasonic vibrations to electrolyte in an existing laboratory ECM system was developed in this study. This experimental system used horizontal orientation of tool and workpiece and pulsed power for better flushing of ECM by-products.

1. Intense ultrasonic vibration of electrolyte negatively affected the rate of ionization, thereby reducing MRR of ECM'ed holes.
2. The intense cavitation caused improved de-agglomeration of ECM by-products to improve flushing and this reduced the wear on the side gap of holes, reducing taper angle. Use of pulse current also improved the flushing of ECM by-products to increase MRR and reduce taper angle of hole.
3. De-passivation of anodic films during ECM significantly made uniform material removal possible and reduced the surface roughness.
4. As expected, as higher peak current increased the material removal rate. A slower feed-rate resulted in more overcut due to stray current, effectively increasing the MRR.
5. Linear regression models were generated for two levels of each process variable in this study. The models were generated for two output parameters, MRR and R_a, with R^2 values 66 % and 94% respectively.

Based on this study, the following avenues should be considered for future work:

- The effect of ultrasonic vibration of electrolyte of MRR can be better understood with a closed loop experimental system which monitors gap continuously.

- It is possible that highly intense cavitation negatively affects anodic reaction and hence the MRR. Lower amplitude range of ultrasonic vibration should be investigated to seek improvement in MRR.
- A more thorough experimental investigation of this new method of ultrasonic vibration is required. Completely randomized experimentation will confirm the absence of bias in the results. Use of more levels and estimation of curvature will give more accurate models.
- Use of other materials as workpiece will give further insight into effect of process parameters.
- The effect of higher range of DC pulse frequency (of the order kHz and above) combined with ultrasonic vibration on quality of holes should be investigated.

REFERENCES

34450A Digital Multimeter, 5 ½ Digit | Keysight (formerly Agilent Electronic Measurement). (2016). Retrieved 7 September, 2016, from http://www.keysight.com/en/pd-2193855-pn-34450A/digital-multimeter-5-1-2-digit?cc=US&lc=eng

A621 A622 Current Probes Datasheet | Tektronix. (2016). from http://www.tek.com/datasheet/a621-a622-current-probes-datasheet

Aglyamov, S. R., Karpiouk, A. B., Bourgeois, F., Ben-Yakar, A., & Emelianov, S. Y. (2008). Ultrasound measurements of cavitation bubble radius for femtosecond laser-induced breakdown in water. *Optics Letters, 33*(12), 1357-1359.

Alicona That's metrology: InfiniteFocus. (2016). Retrieved 7 September, 2016, from http://www.alicona.com/products/infinitefocus/

Bhattacharyya, B., Malapati, M., Munda, J., & Sarkar, A. (2007). Influence of tool vibration on machining performance in electrochemical micro-machining of copper. *International Journal of Machine Tools and Manufacture, 47*(2), 335-342.

Bhattacharyya, B., Munda, J., & Malapati, M. (2004). Advancement in electrochemical micro-machining. *International Journal of Machine Tools and Manufacture, 44*(15), 1577-1589.

Branson Ultrasonic SLP Cell Disruptor 150 watts 117V 101-063-726. (2016). Retrieved 7 September, 2016, from http://www.eraymedical.com/branson-ultrasonic-slp-cell-disruptor-101-063-726.html?utm_source=googlepepla&utm_medium=adwords&id=70740923505

Capelo-Martinez, J.-l. (2009). *Ultrasound in chemistry: Analytical applications*: John Wiley & Sons.

Branson Ultrasonic Corporation (2007). Sonifier Cell Disrupter Model SLPe User's Manual Rev A. Retrieved July 12, 2016, from

http://pdfs.wolflabs.co.uk/service/Branson%20_Sonicators_-_100-214-254_A_Sonifier.pdf

Ebeid, S. J., Hewidy, M. S., El-Taweel, T. A., & Youssef, A. H. (2004). Towards higher accuracy for ECM hybridized with low-frequency vibrations using the response surface methodology. *Journal of Materials Processing Technology, 149*(1-3), 432-438.

Fluke 45 Dual Display Multimeter. (2016). Retrieved 7 September, 2016, from http://www.fluke.com/fluke/m3en/digital-multimeters/fluke-45.htm?pid=56082

Han, M.-S., Min, B.-K., & Lee, S. J. (2009). Geometric improvement of electrochemical discharge micro-drilling using an ultrasonic-vibrated electrolyte. *Journal of Micromechanics and Microengineering, 19*(6), 065004.

Hielscher, T. (2007). Ultrasonic production of nano-size dispersions and emulsions. *arXiv preprint arXiv:0708.1831*.

Hoar, T. (1967). The production and breakdown of the passivity of metals. *Corrosion Science, 7*(6), 341-355.

Kuttruff, H. (2012). *Ultrasonics: Fundamentals and applications*: Springer Science & Business Media.

LaBoda, M., & McMillan, M. (1967). A new electrolyte for electrochemical machining. Pt. 1. Developmental studies. *Electrochem Tech, 5*(7), 340-346.

Li, H., Afacan, A., Liu, Q., & Xu, Z. (2015). Study interactions between fine particles and micron size bubbles generated by hydrodynamic cavitation. *Minerals Engineering, 84*, 106-115.

Mason, T. (2000). *Sonochemistry, Chemistry primers*: Oxford.

Mason, T. J. (2016). Ultrasonic cleaning: An historical perspective. *Ultrason Sonochem, 29*, 519-523.

Mason, T. J., & Peters, D. (2002). *Practical sonochemistry: Power ultrasound uses and applications*: Woodhead Publishing.

McGeough, J. (1971). Some effects of carbon content on the efficiency of electrochemically machined carbon steels and cast iron. *The International Journal of Production Research, 9*(2), 311-316.

McGeough, J. A. (1974). *Principles of electrochemical machining*: Chapman and Hall.

McGeough, J. A. (2005). Electrochemical machining. *Kirk-Othmer Encyclopedia of Chemical Technology*.

McQueen, D. (1986). Frequency dependence of ultrasonic cleaning. *Ultrasonics, 24*(5), 273-280.

Mitchell-Smith, J., & Clare, A. T. (2016). Electrochemical jet machining of Titanium: Overcoming passivation layers with ultrasonic assistance. *Procedia CIRP, 42*, 379-383.

Mukherjee, S. K., Kumar, S., Srivastava, P. K., & Kumar, A. (2008). Effect of valency on material removal rate in electrochemical machining of aluminium. *Journal of Materials Processing Technology, 202*(1-3), 398-401.

Nicoară, D., Hedeş, A., & Şora, I. (2006). *Ultrasonic Enhancement of an Electrochemical Machining Process.* Paper presented at the Proceedings of the 5th WSEAS international conference on Applications of electrical engineering.

Niemczewski, B. (1980). A comparison of ultrasonic cavitation intensity in liquids. *Ultrasonics, 18*(3), 107-110.

Pa, P. S. (2006). Design of effective plate-shape electrode in ultrasonic electrochemical finishing. *The International Journal of Advanced Manufacturing Technology, 34*(1-2), 70-78.

Pa, P. S. (2007). Electrode form design of large holes of die material in ultrasonic electrochemical finishing. *Journal of Materials Processing Technology, 192-193*, 470-477.

Pa, P. S. (2009). Super finishing with ultrasonic and magnetic assistance in electrochemical micro-machining. *Electrochimica Acta, 54*(25), 6022-6027.

Postlethwaite, J., & Kell, A. (1972). Periodic phenomena during the anodic dissolution of iron in sodium chloride solutions. *Journal of The Electrochemical Society, 119*(10), 1351-1352.

Powers, R. (1971). Film Formation and Hydrogen Evolution on the Alkaline Zinc Electrode. *Journal of the Electrochemical Society, 118*(5), 685-695.

PowerTIG 255EXT - TIG Welders | Everlast Generators. (2016). Retrieved 7 September, 2016, from http://www.everlastgenerators.com/product/tig-stick/powertig-255ext

Racicot, R., Yang, S., & Brown, R. (1996). *Evidence of a passive layer formation from a conductive polymer coating on aluminum alloys.* Paper presented at the MRS Proceedings.

Rajurkar, K. P., Wei, B., Kozak, J., & McGeough, J. (1995). Modelling and monitoring interelectrode gap in pulse electrochemical machining. *CIRP Annals-Manufacturing Technology, 44*(1), 177-180.

Rao, S. R., Padmanabhan, G., Naidu, K. M., & Reddy, A. R. (2014). Parametric study for radial over cut in Electrochemical drilling of Al-5% B 4 C p Composites. *Procedia Engineering, 97*, 1004-1011.

Ruszaj, A., Skoczypiec, S., Czekaj, J., Miller, T., & Dziedzic, J. (2007). *Surface micro and nanofinishing using pulse electrochemical machining process assisted by electrode ultrasonic vibrations.* Paper presented at the Proceedings of the 15th International Symposium on Electromachining–ISEM XV, April.

Ruszaj, A., Zybura-Skrabalak, M., Skoczypiec, S., & Żurek, R. (2001). *Electrochemical machining supported by electrode ultrasonic vibrations.* Paper presented at the 13th International Symposium for Electromachining.

Ruszaj, A., Zybura, M., Zurek, R., & Skrabalak, G. (2003). Some aspects of the electrochemical machining process supported by electrode ultrasonic vibrations optimization. *Proceedings of the Institution of Mechanical Engineers Part B-Journal of Engineering Manufacture, 217*(10), 1365-1371.

Ryu, S. H. (2015). Eco-Friendly ECM in citric Acid electrolyte with microwire and microfoil Electrodes. *International Journal of Precision Engineering and Manufacturing, 16*(2), 233-239.

Sebastian, S., Adam, R., Jan, C., & Maria, Z. S. (2003). *Primary investigations on USECM–CNC process.* Paper presented at the 18th International Conference on Computer - Aided Production Engineering, Edinburgh, UK.

Serway, R. A., & Jewett, J. W. (2013). *Physics for scientists and engineers with modern physics*: Nelson Education.

Skoczypiec, S. (2010). Research on ultrasonically assisted electrochemical machining process. *The International Journal of Advanced Manufacturing Technology, 52*(5-8), 565-574.

Skoczypiec, S., & Ruszaj, A. (2005). Discussion of cavitation phenomena influence on electrochemical machining process. *Int J Manuf Sci Technol, 7*(2), 27-32.

Swain, A., Sundaram, M., & Rajurkar, K. P. (2012). Use of coated microtools in advanced manufacturing: An exploratory study in electrochemical machining (ECM) context. *Journal of Manufacturing Processes, 14*(2), 150-159.

Tak, Y., Henderson, E. R., & Hebert, K. R. (1994). Evolution of microscopic surface topography during passivation of aluminum. *Journal of the Electrochemical Society, 141*(6), 1446-1452.

Velmex Motor Controllers - VXM. (2016). Retrieved 7 September, 2016, from http://www.velmex.com/Products/Controls/VXM_Controller.html

Velmex Motorized BiSlide Systems. (2016). Retrieved 7 September, 2016, from http://www.velmex.com/Products/BiSlide/BiSlide_Motorized.html

Verhaagen, B., & Fernandez Rivas, D. (2016). Measuring cavitation and its cleaning effect. *Ultrason Sonochem, 29*, 619-628.

Wang, M., Zhang, Y., He, Z., & Peng, W. (2016). Deep micro-hole fabrication in EMM on stainless steel using disk micro-tool assisted by ultrasonic vibration. *Journal of Materials Processing Technology, 229*, 475-483.

Wang, W., Zhu, D., Qu, N., Huang, S., & Fang, X. (2010). Electrochemical drilling with vacuum extraction of electrolyte. *Journal of Materials Processing Technology*, *210*(2), 238-244.

Wess, O. (2006). *Physics and technology of shock wave and pressure wave therapy.* Paper presented at the 9th International Congress of the International Society for Musculoskeletal Shockwave Therapy (ISMST). News Letter ISMST.

Xi, X., Cegla, F. B., Lowe, M., Thiemann, A., Nowak, T., Mettin, R., . . . Lippert, A. (2011). Study on the bubble transport mechanism in an acoustic standing wave field. *Ultrasonics, 51*(8), 1014-1025.

Yusof, N. S., Babgi, B., Alghamdi, Y., Aksu, M., Madhavan, J., & Ashokkumar, M. (2016). Physical and chemical effects of acoustic cavitation in selected ultrasonic cleaning applications. *Ultrason Sonochem, 29*, 568-576.

Zijlstra, A., Fernandez Rivas, D., Gardeniers, H. J., Versluis, M., & Lohse, D. (2015). Enhancing acoustic cavitation using artificial crevice bubbles. *Ultrasonics, 56*, 512-523.

APPENDIX A: COSMOS PROGRAMS

1. **IEG setting:** This program moves the tool 0.3 mm from the workpiece surface to give starting IEG.

F C S1M1000, I1M-120, R

Command	Meaning
F	Start
C	Cancel previous commands
S1M1000	Motor 1 set to move at the speed of 1000 steps[*1]/s
I1M-120	Motor 1 moves 120 steps in backward direction
R	End

[1] Each step equals 2.5 μm

2. **Drilling at low feed-rate:** This program moves the tool 6.2 mm in the direction of the workpiece surface at 10 µm/s

F C S1M4, I1M2480, S1M1000, I1M-2480, R

Command	Meaning
F	Start
C	Cancel previous commands
S1M4	Motor 1 set to move at the speed of 4 steps/s
I1M2480	Motor 1 moves 2480 steps in forward direction
S1M1000	Motor 1 set to move at the speed of 1000 steps/s
I1M-2480	Motor 1 moves 2480 steps in backward direction
R	End

3. **Drilling at high feed-rate:** This program moves the tool 6.2 mm in the direction of the workpiece surface at 15 µm/s.

F C S1M5, I1M2480, S1M1000, I1M-2480, R

Command	Meaning
F	Start
C	Cancel previous commands
S1M5	Motor 1 set to move at the speed of 5 steps/s
I1M2480	Motor 1 moves 2480 steps in forward direction
S1M1000	Motor 1 set to move at the speed of 1000 steps/s
I1M-2480	Motor 1 moves 2480 steps in backward direction
R	End

APPENDIX B: DESCRIPTION OF COMPONENTS

Velmex BiSlide positioning system and VXM controller

The Velmex Bi-Slide system is a positioning system of high accuracy. The lead screw resolution is 0.00025” and its repeatability is 0.00015” ("Velmex Motorized BiSlide Systems," 2016). The load carrying capacity of Velmex Bi-slide is up to 300 lbs. It uses PTFE bearings which give smoother movement and less friction. It operates without lubrication and it uses strong I-beam cross section made of hard aluminum.

The stepper motors that control the X and Z axis motion of the Bi-Slide can be programmed to move a specific distance at a specific speed in those axes. This is accomplished by COSMOS software. Manual operation of motors is done using a controller provided for the same.

In case of emergency during running a programmed motion of the motors, the motion can be stopped to avoid any damage or losses. The tool and the ultrasonic probe was mounted on the Bi-Slide by designing and fabricating appropriate holder. This enabled the servo-motors to move the tool and the ultrasonic probe at the desired feed rate and drill holes of desired depth.

The servomotor motion is programmed in order to have a constant feed-rate into the workpiece.

Figure 54: (A) Velmex Bislide Positioning System ("Velmex Motorized BiSlide Systems," 2016) (B) VXM Controller System ("Velmex Motor Controllers - VXM," 2016)

Everlast 255 Ext DC power supply

The power supply is a constant current. The specific name of the model is PowerTIG 255EXT/324 EXT TIG/ Stick Welder. The Welder has AC/DC capacity and is controlled by Digital Microprocessor. It is capable of Advanced Soft Square, Soft Square Sine and triangular AC wave forms. The starting current range is 5-250 A for AC and DC. The ending current range is 3-250 A for DC and 5-250 for AC. It is also capable of pulsed frequency in DC (1-500Hz), Advanced AC square wave (0.1-10Hz) and AC (1-250 Hz). For the experiments 'Normal' EasyStart Up setting is used to work with standard set-up. Since this power source is not being used for welding, no preflow is needed and is set at 0 seconds.

The upslope setting for the power source is set at 0 seconds (available 0-25 seconds). This indicates the amount of time taken from escalating from initial amperage to the welding amp value. The welding amps represent the peak value of amperage.

Pulse on-time represents the amount of time the current is in the “welding” stage compared to the background current stage.

The pulse current setting controls the background current as a percentage value of the peak current. This indicates the drop in current at each pulse. This is set at 50 µm duty cycle.

Pulse frequency setting determines the number of on-time off-time cycles achieved in a single second. This setting has options between 1-500Hz for DC Voltage. Note that at higher pulse frequency the noise level of the power source is high and higher protection is recommended.

The end amps set the final amperage value before the power source stops transmitting current.

The pulse mode selector offers three modes: Pulse OFF, Standard Pulse and Advanced AC pulse. The mode used is Standard mode (in DC voltage). The advanced pulse mode works only with AC voltage. Pulse setting controls the heat input during power transmission.

The 2T option is just a press and hold option, which starts the cycle automatically.

To operate with pedal, the same sequence applies once “pedal mode” is selected. Since there no pre-flow or post flow required in ECM, we select the 2T option.

The waveform selected is DC since the ECM experiments are going to be on pulse DC power.

Purge Gas is used to provide additional cooling post welding (for welding applications). For this case, purge gas flow is set to “off”.

Figure 55: Pulsed DC Power Source For ECM System ("PowerTIG 255EXT - TIG Welders | Everlast Generators," 2016)

Longer WT600-2J peristaltic pump

Two Longer WT2600-2J pumps with KZ25 pump heads were used to pump electrolyte through the tool into ECM bath and also pump out the collected electrolyte from the bath. This pump works on a DC brushless motor. The flow rate of this pump ranges from 4.2 to 6000 ml/min. The key advantages of this pump are low vibration which is essential for a rigid ECM system and low maintenance which is important because of the risk of corrosion.

Figure 56: One Unit of Longer Peristaltic Pump for Electrolyte Circulation with KZ25 Pump Head

Branson SLPe ultrasonic probe system

The Branson SLPe ultrasonic system has constant frequency of 40 kHz and operates with a removable microtip 0.125 in diameter. The microtip gives adjustable amplitude in the range of 12 μm – 68 μm.

The tip was inserted at the nodal point into the electrolyte flow path. The amplitude is zero at nodal point so this ensures that there is negligible rubbing of vibrating probe with the Styrofoam packing.

Figure 57: Branson SLPe Ultrasonic Probe System ("Branson Ultrasonic SLP Cell Disruptor 150 watts 117V 101-063-726," 2016)

Fluke 45 multimeter and Tektronic current probe

The Tektronix A662 current probe is connected to Fluke 45 digital multimeter to monitor current by converting it on voltage scale as follows: 10 mV = 1A.

Figure 58: Current Monitoring Using (A) Tektronix Current Probe ("A621 A622 Current Probes Datasheet | Tektronix," 2016) and Fluke45 Multimeter ("Fluke 45 Dual Display Multimeter," 2016)

Keysight 34450 multimeter

Keysight multimeter was used to monitor voltage during ECM drilling process. The voltage data was logged using BenchVue software. The multimeter was switched on few seconds after the machining process started and switched of few seconds before the end of machining cycle. This was done to avoid damage to multimeter. Multimeter was used in high-impedance mode to further protect it from surges due to high current of power source.

Figure 59: Keysight Multimeter For Voltage Monitoring ("34450A Digital Multimeter," 2016)

Alicona IF 3D profiler

The Alicona IF measurement system is a non-contact type of 3D profiler and works on the principle of focus variation. 5X and 10X magnification lens are available for measurement of form and roughness. This profiler was used to generate 3D models for holes and then volume of the holes was measured to calculate MRR. It was also used to generate surface roughness and taper angle of the hole.

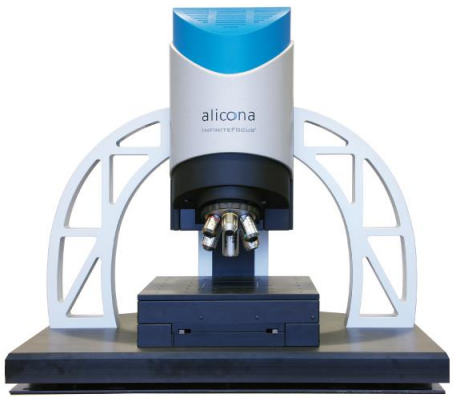

Figure 60: Alicona IF 3D Profiler ("Alicona InfiniteFocus," 2016)

Mitutoyo Vision System and Olympus Optical Microscope

The Mitutoyo Vision System and Olympus microscope were used to calibrate Alicona IF volume measurement module by measuring dimensions of different known shapes and then using formulae to calculate their volumes.

The high magnification and imaging of the Olympus of the microscope was also used to take images of the cross-section of the ECM'ed holes.

APPENDIX C: MRR DATA

The following table contains line MRR measurements for all design points on which experiments were performed.

Experimental Run No.	Amplitude (%)	Peak Current (A)	Pulse Frequency (Hz)	Feed Rate (µm/s)	Volume Removed (mm^3)		Machining Time (minutes)	MRR (mm^3/min)		Average MRR (mm^3/min)
					1	2		1	2	
1	15	22	125	15	153.09	149.53	6.88	22.25	21.73	21.99
2	15	22	125	10	320.16	323.13	10.33	30.99	31.28	31.14
3	15	22	275	15	228.97	223.97	6.88	33.28	33.28	33.28
4	15	22	275	10	312.34	310.65	10.33	30.24	30.07	30.15
5	15	26	125	15	202.98	192.36	6.88	29.50	27.96	28.73
6	15	26	125	10	321.45	330.88	10.33	31.12	32.03	31.57
7	15	26	275	15	210.04	221.59	6.88	30.53	32.21	31.37
8	15	26	275	10	332.88	335.29	10.33	32.22	32.46	32.34

Experimental Run No.	Amplitude (%)	Peak Current (A)	Pulse Frequency (Hz)	Feed Rate (µm/s)	Volume Removed (mm^3)		Machining Time (minutes)	MRR (mm^3/min)		Average MRR (mm^3/min)
					1	2		1	2	
9	45	22	125	15	138.64	137.29	6.88	20.15	19.95	20.05
10	45	22	125	10	292.63	300.17	10.33	28.33	29.06	28.69
11	45	22	275	15	210.98	210.98	6.88	30.67	30.67	30.67
12	45	22	275	10	305.88	307.76	10.33	29.61	29.79	29.70
13	45	26	125	15	197.73	183.50	6.88	28.74	26.67	27.71
14	45	26	125	10	319.73	317.53	10.33	30.95	30.74	30.84
15	45	26	275	15	191.92	180.27	6.88	27.90	26.20	27.05
16	45	26	275	10	317.00	320.12	10.33	30.69	30.99	30.84

Experimental Run No.	Amplitude (%)	Peak Current (A)	Pulse Frequency (Hz)	Feed Rate (µm/s)	Volume Removed (mm^3)		Machining Time (minutes)	MRR (mm^3/min)		Average MRR (mm^3/min)
					1	2		1	2	
17	0	22	125	15	203.46	198.50	6.88	29.57	28.85	29.21
18	0	22	125	10	327.84	325.00	10.33	31.74	31.46	31.60
19	0	22	275	15	229.39	232.13	6.88	33.34	33.74	33.54
20	0	22	275	10	334.24	334.78	10.33	32.36	32.41	32.38
21	0	26	125	15	237.49	237.65	6.88	34.52	34.54	34.53
22	0	26	125	10	331.58	330.41	10.33	32.10	31.99	32.04
23	0	26	275	15	259.13	261.22	6.88	37.66	37.97	37.82
24	0	26	275	10	391.75	378.13	10.33	37.92	36.60	37.26
25	0	22	10	15	206.16	203.66	6.88	29.96	29.60	29.90

Experimental Run No.	Amplitude (%)	Peak Current (A)	Pulse Frequency (Hz)	Feed Rate (µm/s)	Volume Removed (mm^3)		Machining Time (minutes)	MRR (mm^3/min)		Average MRR (mm^3/min)
					1	2		1	2	
25	0	22	0	15	202.34	207.06	6.88	29.41	30.10	29.75
26	10	22	0	15	201.72	197.91	6.88	29.32	28.77	29.04
28	45	22	0	15	212.95	208.51	6.88	30.95	30.31	30.63

APPENDIX D: SURFACE ROUGHNESS DATA

The following table contains line average surface roughness measurements for all design points on which experiments were performed.

Experimental Run No.	Amplitude (%)	Peak Current (A)	Pulse Frequency (Hz)	Feed Rate (µm/s)	Surface Roughness- Ra										Average Ra (µm)
					Sample 1					Sample 2					
					1	2	3	4	5	1	2	3	4	5	
1	15	22	125	15	1.09	1.87	1.40	1.55	1.14	1.52	1.04	1.49	1.66	1.37	1.41
2	15	22	125	10	1.33	1.17	1.46	1.48	1.34	1.46	1.29	1.17	1.32	1.41	1.34
3	15	22	275	15	1.10	1.20	0.74	0.90	0.91	1.05	1.35	1.16	1.21	1.08	1.07
4	15	22	275	10	1.15	0.88	1.10	0.98	1.02	0.99	0.99	0.94	1.01	1.00	1.00
5	15	26	125	15	0.86	0.74	0.96	0.72	1.14	0.98	0.97	0.94	0.84	0.91	0.90
6	15	26	125	10	1.22	1.61	1.37	1.55	1.55	1.32	1.15	1.20	1.15	1.15	1.33
7	15	26	275	15	0.86	0.72	0.93	0.71	0.92	0.67	0.82	0.99	0.85	1.04	0.85
8	15	26	275	10	1.10	1.14	1.22	1.17	1.21	1.22	1.10	1.12	1.06	1.41	1.17

Experimental Run No.	Amplitude (%)	Peak Current (A)	Pulse Frequency (Hz)	Feed Rate (µm/s)	Surface Roughness- Ra										Average Ra (µm)
					Sample 1					Sample 2					
					1	2	3	4	5	1	2	3	4	5	
9	45	22	125	15	1.48	1.32	1.01	1.23	1.29	0.97	1.47	1.38	1.06	1.20	1.24
10	45	22	125	10	1.24	1.90	1.54	1.47	1.36	1.44	1.35	1.20	2.01	1.22	1.47
11	45	22	275	15	1.93	1.99	1.66	1.91	1.90	1.43	1.76	1.49	1.50	1.38	1.69
12	45	22	275	10	1.70	1.88	1.93	1.56	1.68	2.63	1.95	1.76	1.44	1.87	1.84
13	45	26	125	15	1.43	1.53	1.65	1.11	1.31	1.41	1.40	1.38	1.32	1.36	1.39
14	45	26	125	10	3.62	2.93	1.77	2.65	3.21	2.43	1.76	1.99	2.11	1.50	2.40
15	45	26	275	15	1.06	1.22	1.06	1.85	0.86	0.97	0.84	1.21	1.13	0.87	1.11
16	45	26	275	10	2.35	2.12	2.16	1.18	3.12	1.78	3.13	2.72	3.87	2.20	2.46

Experimental Run No.	Amplitude (%)	Peak Current (A)	Pulse Frequency (Hz)	Feed Rate (µm/s)	Surface Roughness- Ra										Average Ra (µm)
					Sample 1					Sample 2					
					1	2	3	4	5	1	2	3	4	5	
17	0	22	125	15	1.40	2.72	1.98	2.42	2.33	1.40	2.33	2.34	2.46	2.18	2.16
18	0	22	125	10	1.82	3.00	2.91	1.91	4.12	2.54	3.99	3.91	3.76	3.84	3.18
19	0	22	275	15	2.49	2.06	2.58	2.46	2.59	1.69	1.72	4.12	1.82	3.78	2.53
20	0	22	275	10	3.63	3.95	3.79	3.81	3.02	1.97	1.92	3.42	3.70	1.79	3.10
21	0	26	125	15	1.74	2.25	4.48	4.33	1.75	2.30	2.79	2.68	3.19	3.56	2.91
22	0	26	125	10	3.08	3.17	3.33	3.08	3.08	3.42	2.57	4.08	1.99	3.13	3.09
23	0	26	275	15	1.14	2.80	2.81	4.32	2.08	3.15	2.45	2.96	2.99	2.82	2.75
24	0	26	275	10	3.54	3.45	3.27	3.91	2.10	3.76	3.38	3.38	2.51	3.33	3.26

Experimental Run No.	Amplitude (%)	Peak Current (A)	Pulse Frequency (Hz)	Feed Rate (µm/s)	Surface Roughness- Ra										Average Ra (µm)
					Sample 1					Sample 2					
					1	2	3	4	5	1	2	3	4	5	
25	0	22	0	15	1.74	1.88	2.10	1.81	1.88	1.82	1.94	2.58	1.82	2.17	1.97
26	15	22	0	15	1.18	1.25	0.97	1.28	1.05	0.91	0.93	1.05	0.93	0.99	1.05
27	45	22	0	15	1.09	1.11	1.25	0.95	1.01	1.05	1.00	0.86	0.92	1.10	1.03

The following table consists of selected measurements for mean peak surface roughness (R_z). These measurements are for holes ECM'ed at 22 A I_p and 15 µm/s f_r.

Amplitude (%)	Peak Current (A)	Pulse Frequency (Hz)	Feed Rate (µm/sec)	Surface Roughness- Rz (µm)										Average R_z (µm)
				Sample 1					Sample 2					
				1	2	3	4	5	1	2	3	4	5	
15	22	125	15	4.14	3.28	3.82	4.69	3.39	4.64	2.12	4.79	3.63	2.19	3.67
15	22	275	15	2.63	2.32	2.80	3.35	3.15	4.06	5.41	2.30	2.03	3.29	3.13
45	22	125	15	4.91	4.73	5.92	6.06	9.28	5.88	5.36	6.66	7.14	4.87	6.08
45	22	275	15	3.96	4.58	5.07	3.55	4.05	4.69	4.15	5.24	2.09	2.97	4.04
0	22	125	15	11.06	10.09	10.00	8.02	11.40	10.16	9.22	9.82	9.81	8.56	9.81
0	22	275	15	13.03	17.93	8.48	8.79	13.49	8.53	12.90	12.86	13.10	13.65	12.28
0	22	0	15	6.93	7.43	16.83	7.59	11.20	9.22	10.53	14.06	16.24	14.69	11.47
15	22	0	15	2.90	2.81	2.41	3.26	2.94	2.55	3.31	2.66	2.82	3.89	2.96
45	22	0	15	3.70	2.47	3.44	3.29	3.45	3.59	3.38	2.85	3.47	3.76	3.34

APPENDIX E: TAPER ANGLE DATA

Following table contains the taper angle measurements of the holes ECM'ed at 22 A I_p and 15 µm/s f_r. The measurement of the taper angle was at 5 different locations in the "12 'o' clock" region.

DC Pulse Frequency (Hz)	Ultrasonic Vibration Amplitude (%)	Taper Angle (Degrees)					Average Taper Angle (Degrees)
		1	2	3	4	5	
0	0	10.75	10.41	14.22	10.76	8.82	10.99
125	0	2.30	2.02	3.28	2.87	3.13	2.72
275	0	1.88	2.09	2.91	2.17	2.48	2.31
0	15	5.77	1.74	2.52	5.62	3.59	3.85
125	15	2.79	1.44	1.41	1.40	1.39	1.69
275	15	0.35	0.82	0.13	0.94	1.19	0.69
0	45	5.30	2.48	8.41	4.43	5.59	5.24
125	45	1.82	0.60	0.84	2.15	1.97	1.47
275	45	0.79	0.60	1.27	0.79	0.94	0.88